Performance of aerosol optical depth forecasts over the Middle East: Multi-model analysis and validation

Jared A. Lee[1], Christian A. Gueymard[2], and Pedro A. Jiménez[1]

[1] Research Applications Laboratory, National Center for Atmospheric Research, Boulder, CO, USA

[2] Solar Consulting Services, Colebrook, NH, USA

Key Points:

1. Accurate forecasts of aerosol optical depth are crucial for accurate solar irradiance and solar power forecasts in clear-sky conditions
2. Two years of aerosol optical depth forecasts from three global models are validated against ground-based observations in the Middle East
3. Forecast model performance during two significant dust storm events in the UAE and Kuwait is also examined

Keywords: Aerosol optical depth, AERONET, Middle East, dust forecasts, solar irradiance forecasting, solar power

Corresponding author: Dr. Jared A. Lee (jaredlee@ucar.edu), ORCiD 0000-0002-8841-0738

Article submitted to *Journal of Geophysical Research: Atmospheres* on 10 March 2021

Abstract

A primary source of error for predictions of solar irradiance in clear-sky conditions is the total aerosol optical depth (AOD). Dust aerosol loading can also be significant in arid regions such as the Middle East, thus considerably decreasing the solar resource while increasing the detrimental effects of soiling on collectors at solar power plants, particularly during dust storms. Many photovoltaic (PV) and concentrated solar power (CSP) plants have been or will be constructed in the Middle East, making AOD forecasting a pressing issue for plant and grid operators. In this study we present a climatological analysis of 1–3-day AOD forecasts from a two-year period (2018–2019) from three operational models: the NASA Goddard Earth Observing System Model, Version 5 (GEOS-5), the NEMS GFS Aerosol Component (NGAC) model, and the Copernicus Atmosphere Monitoring Service (CAMS) Near-Real-Time (NRT) model. AOD predictions from these models are validated against daily-average observations from 20 Aerosol Robotic Network (AERONET) stations across the Middle East. It is found that GEOS-5 is the best model on average, with the smallest fractional gross error and near-zero modified normalized mean bias. CAMS NRT is the next-best model, while NGAC, which has the coarsest grid spacing of the three models examined here, generally performs poorly. In addition to standard error metrics to characterize the overall performance of the models, a multi-site time series analysis is performed to assess how well these models represent significant dust storm events in the UAE in July 2018 and in Kuwait in April 2018.

42 **Plain Language Summary**

43 Dust, soot, sea salt, and other particles (aerosols) in the atmosphere absorb, reflect, and
44 scatter solar radiation. During clear, sunny conditions, the total amount of atmospheric
45 aerosols controls how much solar irradiance reaches the surface, and therefore the energy
46 generation at solar power plants. Therefore, accurate forecasts of aerosols are important,
47 especially in dusty, desert regions like the Middle East, where solar power is expected to see
48 major growth in the coming years.

49 In this study we compared total aerosol forecasts in the Middle East from three publicly
50 available models, from NASA and NOAA in the U.S. and from CAMS in Europe. We used
51 forecasts issued twice daily during all of 2018–2019. From each model run we validated the
52 total aerosol forecasts against observations made from 20 ground-based stations across the
53 region. We found that the NASA model performed the best overall in the Middle East, the
54 CAMS model was second-best, and the NOAA model generally performed poorly. Because dust
55 storms are a relatively common phenomenon in the Middle East and bring significant
56 disruptions both to solar power generation and to society in general, we also examined how
57 well the three forecast models performed during two dust storm events.

58

1. Introduction

Aerosols are important and very active constituents of the Earth's atmosphere. Both their direct and indirect effects impact the planetary climate at regional and global scales through radiative forcing (RF). The Fourth Assessment Report of the Intergovernmental Panel on Climate Change (IPCC, 2013) indicates that the net global aerosol RF is estimated at –0.27 W m^{-2}. Some aerosol species, such as black carbon, have a positive RF, whereas sulphates and mineral dust have a negative RF. The overall dust RF is estimated at –0.77 W m^{-2}, which indicates a global cooling effect. Stronger radiative effects (by two orders of magnitude or more at the surface) are typically evaluated locally during powerful dust storms (Alam et al., 2014; Arkian, 2017; Basha et al., 2015; Haywood et al., 2003; Huang et al., 2014; Rémy et al., 2015; Saeed et al., 2014; Sharma et al., 2012). However, it is still difficult to assess the total mass of each aerosol species. According to (IPCC, 2013), mineral dust (1000–4000 Tg y^{-1}) is globally the second largest contributor to the total aerosol load after sea spray (1400–6800 Tg y^{-1}). Nevertheless, over some regions, such as large deserts in the sun belt, dust is by far the dominant natural aerosol species.

Dust affects the regional or global climate in various ways, particularly by interacting with the Earth's energy balance (in terms of both shortwave and longwave radiation), providing cloud condensation nuclei, modifying the radiative properties of clouds, changing precipitation patterns, and altering the wind field (Bangalath & Stenchikov, 2016; Choobari et al., 2014; Huang et al., 2014; Jin et al., 2014; Levin et al., 2005; Osipov & Stenchikov, 2018; Ou et al., 2009; Zhao et al., 2011). Dust storms can affect areas far away from the source regions through long-range transport (Husar et al., 2001; Kaufman et al., 2005; Kim et al., 2014; Kuciauskas et

al., 2018; Middleton, 2017; Prospero et al., 2010; Uno et al., 2009; H. Yu et al., 2012), which makes their precise forecasting important at regional and global scales, and also makes the evaluation of their associated hazards more critical (Middleton, 2017). There is observational evidence that the dust load follows a positive trend in aerosol optical depth (AOD) in various regions, including the Middle East (Alizadeh-Choobari et al., 2016; Hsu et al., 2012; Klingmüller et al., 2016; de Meij et al., 2012; Yoon et al., 2012b, 2012a), although (for this region at least) local downward trends in dust loading can be observed, too (Kokkalis et al., 2018; Modarres & Sadeghi, 2018). For all the considerations summarized above, the overall dust cycle is now considered an important topic in Earth system science (Shao et al., 2011).

This contribution's specific interest for dust aerosols is motivated by three main reasons: (i) their mass and optical properties are highly variable in both space and time, which makes their forecasting challenging; (ii) over arid and desert regions, the incidence of dust storms may have considerable impacts on weather, society, air quality, populations' health, as well as terrestrial and air traffic, etc., which makes such events important to forecast so as to provide the necessary warnings; (iii) in recent years, many countries of the sun belt, most particularly in the Middle East, have begun implementing aggressive energy policies that favor solar technologies to decrease their dependence on oil (Alnaser & Alnaser, 2019; Alsayegh et al., 2018; Lude et al., 2015; Mas'ud et al., 2018; Munawwar & Ghedira, 2014; Poudineh et al., 2018; Salam & Khan, 2017; Seznec, 2018). In this context of rapid transformation of the energy sector, electric utilities now require good production forecasts for all variable sources of renewable energy, particularly solar.

Dust aerosols impact the production of solar power in two different ways: (i) they tend to decrease the solar resource in comparison with temperate areas; and (ii) they tend to deposit on the active surface of solar generators, thus decreasing their output and creating the need for regular cleaning. Because such impacts have serious consequences, the possibility of forecasting them carries important societal and economic value. Over those regions, the aerosol-induced variability in surface irradiance is the primary cause of temporal variability of solar radiation because clouds are relatively infrequent there. Fluctuating cloudiness is prevalent elsewhere and has prompted the development of specialized numerical weather prediction (NWP) models aimed at forecasting the solar irradiance components at the mesoscale (e.g., (Jiménez, Hacker, et al., 2016). Such NWP models are mostly used in temperate climates to forecast the occurrence and intensity of cloudy periods over a relatively small domain. They are now progressively being updated and improved to also take the variability of the aerosol regime into account (Eissa et al., 2018; Thompson & Eidhammer, 2014). In parallel, global weather or climate models need to incorporate detailed modeling of aerosol chemistry and transport, since these modify the solar radiation field, and provide cloud condensation nuclei that ultimately allow the formation of clouds. In recent years, specialized forecast models have been developed and tailored to uniquely evaluate the quantitative evolution of dust aerosols. For instance, (Huneeus et al., 2011) describes the efforts of the AeroCom consortium (https://aerocom.met.no) to improve global dust models. Moreover, the World Meteorological Organization (WMO) has recognized the importance and societal implications of dust storms, which led to the creation of the WMO Sand and Dust Storm Project in 2004 and its Sand and

123 Dust Storm Warning Advisory and Assessment System (SDS-WAS) in 2007. Three SDS-WAS
124 regional centers now exist to provide dust aerosol forecasts over different continents.
125 The main objective here is to validate various aerosol forecasts over the Middle East and
126 better understand the causes for their differences. AOD is the essential variable considered
127 here because it can be directly used to predict the components of surface solar irradiance,
128 which in turn are needed to forecast the power production of any solar power plant. In general,
129 AOD is also viewed as useful to evaluate air quality at the surface through the determination of
130 customary indices (PM_1, $PM_{2.5}$, and PM_{10}), but their correlation with AOD (a columnar quantity)
131 is typically not strong (Filip & Stefan, 2011). In the case of dust storms, however, all dust
132 particles are of large dimension and concentrated in the bottom layers of the atmosphere,
133 making the AOD and PM_{10} better correlated over space (Beegum et al., 2018). Air quality
134 implications of dust storms are extremely important (Ahmady-Birgani et al., 2018; Al-Hemoud
135 et al., 2018, 2019; Middleton, 2017; Querol et al., 2019), but beyond the scope of the present
136 study. AOD can be uniquely determined at each visible wavelength, but is most commonly
137 reported at 550 nm, which is near the peak of the solar visible emission spectrum, and is
138 abbreviated as AOD_{550} in what follows.
139 The current literature indicates a growing interest for the observation and prediction of
140 AOD over the Middle East. Most observations are made through remote sensing either from
141 ground-based sun photometers of, e.g., NASA's federated Aerosol Robotic Network (AERONET)
142 (Holben et al., 1998) or from spaceborne radiometers such as MODIS or MISR (Klingmüller et
143 al., 2016; K. R. Kumar et al., 2018; Y. Yu et al., 2016). Ground-based observations have the
144 lowest uncertainty and are used to validate other products, such as spaceborne observations or

145 modeled values. A number of models now exist to forecast the life cycle and abundance of dust
146 aerosols (Basart et al., 2012; Beegum et al., 2018; Benedetti et al., 2014; Eissa et al., 2018;
147 Ginoux et al., 2001; Huneeus et al., 2011; Lu et al., 2016; Pérez et al., 2011). In the literature,
148 such chemistry transport models are typically used to *retrospectively* simulate the occurrence
149 of known dust storm and compare results (of AOD, PM_{10}, etc.) to observations (Basha et al.,
150 2015; Beegum et al., 2018; Calastrini et al., 2012; Hamidi et al., 2017; Haustein et al., 2012;
151 Huneeus et al., 2016; Karagulian et al., 2019; R. Kumar et al., 2014; Liu et al., 2003; Najafpour et
152 al., 2018; Pérez et al., 2006; Xu, 2018; Zhang et al., 2015). In contrast, the literature is relatively
153 limited with respect to the experimental or operational *forecasting* of AOD or PM_{10} over dust-
154 impacted regions (Basart et al., 2012; Benedetti, Giuseppe, et al., 2019; Eissa et al., 2018; Li et
155 al., 2011; Lu et al., 2016; Mangold et al., 2011; Menut et al., 2015). For that reason, the present
156 contribution focuses on comparing and evaluating the AOD forecasting skill of a number of
157 models over the Middle East.

158 This paper is organized as follows. Section 2 describes the aerosol forecast models that
159 are analyzed here. Section 3 describes the AERONET observations and stations that are used to
160 verify the model forecasts, as well as the evaluation metrics that are used. Results are
161 presented and discussed in Section 4, and Section 5 gives conclusions.
162

163 **2. Aerosol forecasting models**

164 In this study we analyze and compare AOD forecasts from three global models over the
165 Middle East: the NASA Goddard Earth Observing System Model, Version 5 (GEOS-5); the NOAA
166 Environmental Modeling System (NEMS) Global Forecasting System (GFS) Aerosol Component

(NGAC); and the Copernicus Atmosphere Monitoring Service (CAMS) Near-real time global analysis and forecast model. These models are briefly described below. Preliminary analysis shows that they produce wildly different spatial patterns in the AOD_{550} forecasts, which is concerning and justifies further analysis. These differences are investigated in detail below (Section 4).

For each of the three forecast models, all available 0000 and 1200 UTC cycles initialized from 1 January 2018–31 December 2019 are used to provide a full two years of forecasts for analysis. Gridded AOD_{550} values are bilinearly interpolated to the AERONET forecast sites in the Middle East that were active at any point during that time period (see Section 3). Daytime AOD_{550} values are then averaged into day-1, day-2, and day-3 periods, defined as a 24-h period centered at 1200 UTC (i.e., a full calendar day). By this averaging convention, day-1 forecasts are deemed valid at 1200 UTC on the day the forecast was initialized, and day-2 forecasts are valid at 1200 UTC on the day after the forecast was initialized, and so on for day-3. Thus, for 0000 UTC forecast cycles, day-1 forecasts are averaged from 0–24-h lead times (daylight only), while day-2 forecasts are averaged from 24–48-h lead times and day-3 from 48–72-h lead times. For 1200 UTC cycles, only day-2 and day-3 forecasts are defined by this averaging convention, with forecasts averaged from 12–36-h lead times for day-2 and 36–60 h for day-3.

2.1 GEOS-5

GEOS-5 is a full Earth system model with multiple components, including atmospheric chemistry, that is used for both weather and climate applications (Rienecker et al., 2008). The current GEOS-5 atmospheric general circulation model (AGCM) is described in (Molod et al.,

2015). Operationally, GEOS-5 is issued four times per day (0000, 0600, 1200, and 1800 UTC), with AOD_{550} output available hourly on a global 0.3125° x 0.25° grid. The 0000 UTC cycle extends to 10 days, the 1200 UTC cycle to 5 days, and both the 0600 and 1800 UTC cycles extend only to lead time 30 h. Because the 0600 and 1800 UTC cycles are so short, and because GEOS-5 is the only model examined with cycles at those times, those two cycles are excluded here. Considering that the assimilation of ground-based or spaceborne aerosol observations has been shown to significantly help the skill of AOD forecasts (Rubin et al., 2017), GEOS-5, which relies on such assimilations (Buchard et al., 2015), is used here as a benchmark. Most relevant for this study, GEOS-5 assimilates AOD observations from the MODIS/Aqua and MODIS/Terra satellite instruments, bias-corrected and calibrated against AERONET observations (Buchard et al., 2015).

The NASA Goddard Chemistry, Aerosol, Radiation, and Transport (GOCART) model (Chin et al., 2002) is implemented online in GEOS-5 (Colarco et al., 2010, 2014). GOCART simulates a suite of five types of atmospheric aerosols: dust, sea salt, sulfates, black carbon, and organic carbon. Because it is online, the aerosols are fully coupled with the atmospheric model dynamics and thermodynamics. The dust sources and emissions in GEOS-5 are based on the (Ginoux et al., 2001) topographic-based map activated by surface winds, with some modifications based on land use changes and for various scaling constants (Colarco et al., 2010). Eight size bins are used, and dust is removed by several processes, including sedimentation, dry deposition, wet removal, and convective scavenging. The reader is referred to (Colarco et al., 2010) for additional details about the dust optical properties in GEOS-5.

2.2 NGAC

NGAC version 2 (Wang et al., 2018) has been the operational aerosol model at the U.S. National Centers for Environmental Prediction (NCEP) since 7 Mar 2017. NGACv2 forecasts are issued twice daily at 0000 UTC and 1200 UTC out to 5 days, with output on a 1.0° x 1.0° global grid at 3-hourly frequency. The underlying meteorological model is the GFS model that was operational at NCEP in spring 2016, but with a different convection scheme. The meteorological initial conditions are provided by the downscaled Global Data Assimilation System (GDAS) analysis, while the dust and aerosol initial conditions are provided by the previous NGACv2 cycle's 12-h forecast. Except for biomass burning, NGACv2 also uses the GOCART aerosol emissions, including following (Ginoux et al., 2001) for dust emissions, regridded to the NGAC 1.0° grid. The aerosol model in NGACv2 is the same GOCART aerosol module as in GEOS-5 (Colarco et al., 2010, 2014). Additional details about NGACv2 can be found in (Wang et al., 2018).

2.3 CAMS NRT

The CAMS Near-real-time (NRT) global analysis and forecast system for concentrations of aerosols and trace gases dates back to May 2012 (Copernicus, 2020), and is driven by the European Centre for Medium-range Weather Forecasting (ECMWF) Integrated Forecast System (IFS) atmospheric model (ECMWF, 2019). CAMS NRT is run twice daily (0000 UTC and 1200 UTC) with 1-hourly output out to 5 days. (Real-time CAMS NRT data is available in 1-h output, but archived CAMS NRT data is available only in 3-h output. In this study we linearly interpolate the AOD_{550} field from the 3-hourly archived files to 1-hourly frequency.) Since June 2016 the CAMS

NRT grid spacing has been ~40 km, and in July 2019 the number of vertical levels increased from 60 to 137 levels with the upgrade to CAMS IFS cycle 46R1 (Copernicus, 2020; Engelen, 2019; Inness et al., 2019).

For reactive chemistry transport modeling, CAMS NRT employs the IFS(CB05) module (Flemming et al., 2015), which is a modified form of the Carbon Bond 2005 chemistry scheme (CB05) (Huijnen et al., 2010). Whereas the aerosol transport model in GEOS-5 and NGAC both use GOCART, prior to 9 July 2019 tropospheric aerosol modeling in CAMS NRT followed (Morcrette et al., 2009) for forecasts with aerosol data assimilation as described in (Benedetti et al., 2009). This model also has prognostic mass mixing ratio variables for dust, sea salt, sulfates, organic carbon, and black carbon species, and includes aerosol removal processes including sedimentation, wet deposition, and dry deposition for all species. Sea salt and dust aerosols represented by three size bins, and their source functions are driven by 10-m wind. As in GEOS-5 and NGAC, the dust source production in CAMS NRT is based on (Ginoux et al., 2001) modified to fit the three dust size bins in CAMS NRT, and accounts for soil type, soil moisture, vegetation cover, snow cover, and surface wind, with source regions limited to areas with a MODIS-derived climatological background albedo of 0.09–0.52 in a given month (Morcrette et al., 2009; Rémy et al., 2019).

New with the CAMS NRT cycle 46R1 implementation on 9 July 2019 is an online dust emission scheme that follows (Nabat et al., 2012), as well as new nitrate and ammonium aerosol species and several other changes (Engelen, 2019). This dust emission scheme increases total dust emissions and shifts them into larger-diameter bins than in the prior CAMS NRT version. (Engelen, 2019) reports that this change slightly increases dust AOD globally, and more

so in North Africa. Note that the last few months of our evaluation period come after this change in CAMS NRT.

3. Observations

3.1 AERONET Sites

AERONET is a globally federated network of solar irradiance and aerosol observing sites operated by NASA (Holben et al., 1998) (https://aeronet.gsfc.nasa.gov/). Stations are irregularly spaced and provide long-term observation records of water vapor and optical, microphysical, and radiative properties of aerosols for the atmospheric science research and modeling communities, to serve as validation for both models and satellite retrieval algorithms. In the domain of interest for this study, there are 20 AERONET stations that had valid reports during at least portions of the two-year evaluation period. A list of those stations is provided in Table 1, and a photo of the AERONET sun photometer instrument at the Shagaya Park station in Kuwait is shown in Figure 1.

Table 1. Metadata for the AERONET stations used in this study.

Station	Country	Latitude (°N)	Longitude (°E)	Data Levels and Date Ranges	Total Daily Obs
Tuz_Golu_3	Turkey	38.79247	33.46468	L2: 24 Jul 2018–13 Sep 2018	17
IMS-METU-ERDEMLI	Turkey	36.56500	34.25500	L2: 1 Jan 2018–10 Apr 2019 L1.5: 29 Apr 2019–09 May 2019	234
Nicosia	Cyprus	35.14063	33.38135	L2: 03 Feb 2019–1 Jan 2020	271
AgiaMarina_Xyliatou	Cyprus	35.03800	33.05770	L2: 1 Jan 2018–13 Jun 2019 L1.5: 3 Jul 2019–1 Jan 2020	438
CUT-TEPAK	Cyprus	34.67481	33.04275	L2: 1 Jan 2018–27 Jun 2019 L1.5: 7 Oct 2019–2 Jan 2020	485

Migal	Israel	33.23639	35.57828	L2: 17 Jun 2018–3 Oct 2019 L1.5: 4 Oct 2019–30 Dec 2019	476
Technion_Haifa_IL	Israel	32.77587	35.02490	L2: 6 Jan 2018–12 May 2019	157
Weizmann_Institute	Israel	31.90724	34.81053	L2: 4 Jan 2018–23 Jun 2019 L1.5: 24 Jun 2019–2 Jan 2020	502
SEDE_BOKER	Israel	30.85500	34.78222	L2: 2 Jan 2018–5 Apr 2019 L1.5: 29 Apr 2019–2 Jan 2020	592
Eilat	Israel	29.50250	34.91750	L2: 2 Jan 2018–14 Jul 2019 L1.5: 14 Nov 2019–2 Jan 2020	311
Cairo_EMA_2	Egypt	30.08077	31.29007	L2: 2 Jan 2018–30 Jul 2019	481
El_Farafra	Egypt	27.05800	27.99017	L2: 1 Jan 2018–30 Aug 2018	143
Qena_SVU	Egypt	26.19992	32.74703	L2: 21 Dec 2018–24 Oct 2019	270
KAUST_Campus	Saudi Arabia	22.30483	39.10283	L2: 2 Jun 2018–19 Oct 2019 L1.5: 22 Oct 2019–19 Dec 2019	173
IASBS	Iran	36.70500	48.50700	L2: 1 Jan 2018–3 May 2018 L1.5: 15 Mar 2019–2 Jan 2020	218
Shagaya_Park	Kuwait	29.20907	47.06053	L1.5: 1 Jan 2018–29 Oct 2019	519
Kuwait_University	Kuwait	29.32500	47.97100	L1.5: 1 Jan 2018–1 Jan 2020	365
Mezaira	UAE	23.10452	53.75466	L2: 1 Jan 2018–8 May 2018 L1.5: 9 May 2018–20 Apr 2019	427
Masdar_Institute	UAE	24.44160	54.61660	L2: 1 Jan 2018–11 Mar 2019	210
DEWA_ResearchCentre	UAE	24.76685	55.36912	L1.5: 29 Sep 2018–2 Jan 2020	371

Figure 1. AERONET sun photometer at Shagaya Renewable Energy Park in western Kuwait. Photo © 2018 by Jared A. Lee.

3.2 AOD_{550} measurements and quality control

AERONET stations are equipped with a sun photometer that senses the direct solar spectrum through a set of interference filters, whose central wavelengths are appropriately selected to retrieve aerosol and water vapor information. Typically, the spectral AOD is derived at seven or eight wavelengths between 340 and 1640 nm. The retrieval algorithm has been recently updated to version 3, and allows AOD to be retrieved with an accuracy of 0.01–0.02, depending on wavelength (Giles et al., 2019). No AOD measurement is made at 550 nm, however, so that AOD_{550} needs to be retrieved indirectly. This is conventionally done by fitting the spectral AOD retrievals to a linearized version of the empirical Ångström relationship, which can be expressed as:

$$\ln(AOD_{550}) = \ln(AOD_{\lambda}) + \alpha \ln\left(\frac{\lambda}{550}\right) \quad (1)$$

where λ is wavelength (nm), AOD_{λ} represents all spectral AOD values between 440 and 870 nm, and α is the corresponding Ångström exponent, as provided by AERONET.

Ideally, these observations occur every few minutes, but can be spaced hours apart in case of cloud interference. AERONET products at both Level 1.5 (cloud screened) and Level 2 (cloud screened and quality assured) are considered here. Although Level-2 products may be of slightly better quality than Level-1.5 products, they are typically not available at all stations or until many months after the observation time. Relying only on the Level-2 product is desirable, but doing this would have considerably reduced the number of stations and/or shortened the validation period at each of them. Including Level-1.5 data is justified because their accuracy is

much better than that of any AOD forecast. This study focuses on daily-mean AOD_{550} measurements because forecasts are not done at high frequency.

3.3 Evaluation metrics

To evaluate the N AOD_{550} forecasts f_i from the GEOS-5, NGAC, and CAMS models against daily-mean AERONET observations o_i, we use standard metrics like mean bias error (MBE), mean absolute error (MAE), root mean squared error (RMSE), and correlation coefficient (R^2). R^2 is simply the square of the Pearson-r correlation coefficient, which is also reported in some figure headings.

$$R^2 = \left(\frac{\sum_{i=1}^{N}(f_i - \bar{f})(o_i - \bar{o})}{\sqrt{\sum_{i=1}^{N}(f_i - \bar{f})^2 \sum_{i=1}^{N}(o_i - \bar{o})^2}} \right)^2 \quad (2)$$

We primarily use two additional metrics, the modified normalized mean bias (MNMB) and fractional gross error (FGE), which are commonly used in air quality and aerosol model validation (Benedetti, Di Giuseppe, et al., 2019; Rémy et al., 2019; Wagner et al., 2015; S. Yu et al., 2006). MNMB and FGE are employed to better capture model performance at low AOD values, and are essentially normalized versions of MBE and MAE, respectively. Both measures are bounded, symmetric with respect to overestimation and underestimation, and limit the impact of outliers, unlike RMSE. MNMB varies between –2 and +2 with 0 being best, while FGE is bounded by 0 (best) and +2 (worst).

$$MNMB = \frac{2}{N}\sum_{i=1}^{N}\frac{f_i - o_i}{f_i + o_i} \quad (3)$$

$$FGE = \frac{2}{N}\sum_{i=1}^{N}\left|\frac{f_i - o_i}{f_i + o_i}\right| \quad (4)$$

For all these statistics, they are calculated as a function of AERONET station, model start date/time, forecast lead time, and model start time of day. For brevity, MBE, MAE, and RMSE results are not presented in this article.

4. Results and discussion

4.1 Domain average results

First, we examine the domain-average results of daily-average AOD_{550} forecasts by calculating statistics for each forecast cycle, as a sort of time series. For 00 UTC cycles, these statistics combine the day-1 and day-2 lead times, while the other cycles only have valid day-2 forecasts, due to our averaging convention.

The domain-average FGE for each forecast cycle is shown in Figure 2a. For most forecast cycles, the FGE is lowest for GEOS-5, and highest for NGAC, with CAMS NRT forecasts in between. Domain-average FGE values range from 0.13–0.64 (median 0.31) for GEOS-5, 0.14–0.76 (median 0.40) for CAMS NRT, and 0.17–1.30 (median 0.53) for NGAC. In general, the forecast errors are lower in summer and higher in winter. One notable exception is in late June 2018, when all three forecast models had a concurrent jump in forecast errors, with NGAC performing worst. This episode is discussed further below.

Domain-average MNMB values are shown in Figure 2b for each forecast cycle. The best scores overall are for GEOS-5 (range -0.44–0.52), which had a near-zero median MNMB of 0.03. CAMS NRT (range -0.25–0.72) exhibits a generally positive MNMB, with a median of 0.28,

indicating that AOD, and thus aerosol concentrations, were generally higher than observed during the two-year period. In contrast, the NGAC results are highly variable with large biases in both directions at times (range -0.98–1.15), but with a generally negative MNMB, with a median of -0.09. The negative MNMB values indicate that NGAC generally underpredicts AOD compared to observations.

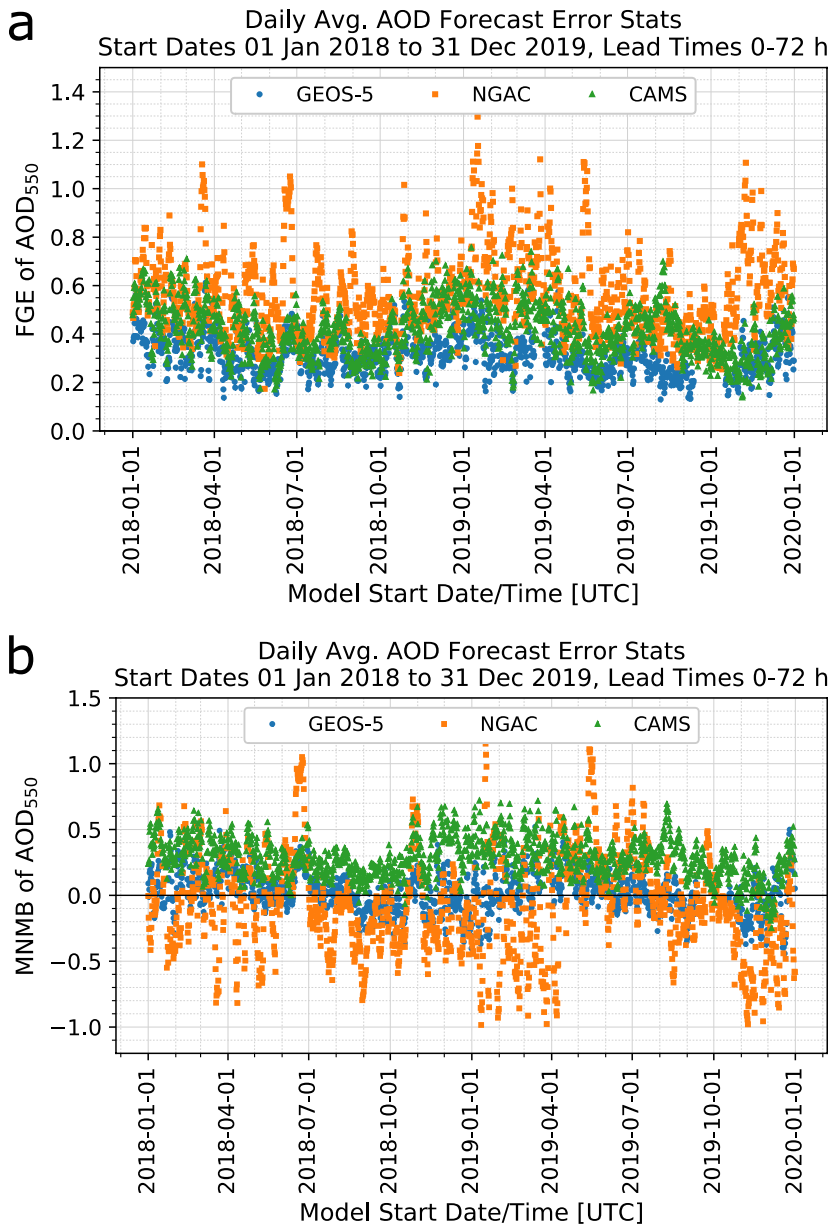

Figure 2. a) Fractional gross error, and b) modified normalized mean bias of daily average AOD_{550} forecasts for each forecast cycle from 1 Jan 2018–31 Dec 2019 for the GEOS-5 (blue circles), NGAC (orange squares), and CAMS NRT (green triangles) models.

The late June 2018 period mentioned above can be seen in Figure 2b with a substantially positive MNMB of around 1.0 during that time for NGAC, and smaller positive MNMB values for GEOS-5 and CAMS NRT, indicating that all the models over-predicted aerosol loading on average during that time period. Additional analysis of the AERONET AOD time series revealed that stations in the eastern Mediterranean (Cyprus, Egypt, and Israel) were primarily responsible for the large positive MNMB overall for NGAC (see Figure 3a for an example), while model-predicted AOD_{550} generally agreed well with AERONET observations in the United Arab Emirates (UAE; e.g., Figure 3b). Moderate positive biases for all models during this time period were observed at AERONET stations in Kuwait (Figure 3c). The substantial differences in AOD_{550} predictions between the three models on 21 June 2018 are displayed in Figure 4, with NGAC predicting a large plume of moderate AOD in the eastern Mediterranean and much of the Fertile Crescent that is completely absent from both GEOS-5 and CAMS NRT, as well as the AERONET observations (Figure 3).

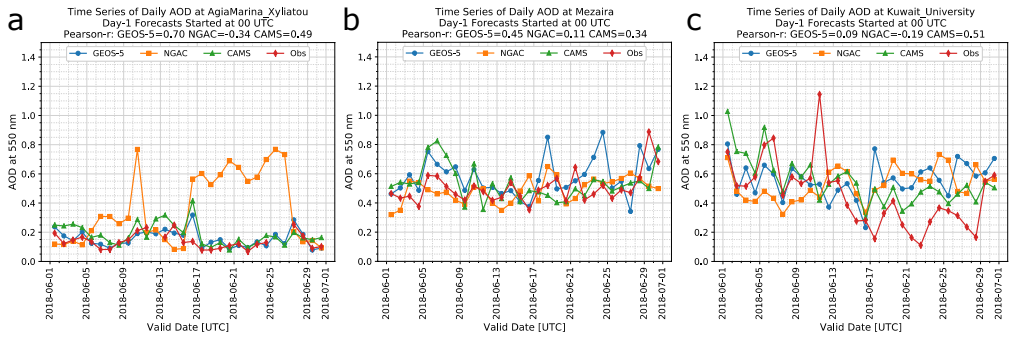

Figure 3. Time series of day-1 daily average AOD_{550} forecasts started at 00 UTC during June 2018 from the GEOS-5 (blue circles), NGAC (orange squares), and CAMS NRT (green triangles) models and observations (red diamonds) from the AERONET stations at a) AgiaMarina_Xyliatou in Cyprus, b) Mezaira in the UAE, and c) Kuwait_University in Kuwait. Pearson-r correlation coefficients for each model are given in the figure title for each panel.

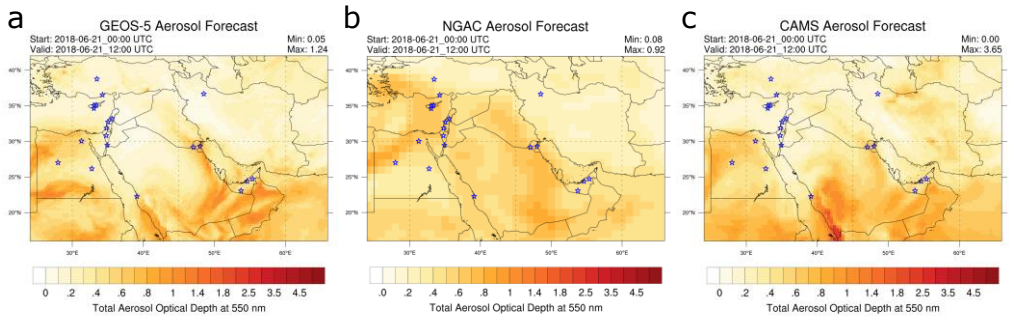

Figure 4. Snapshot of AOD_{550} forecasts issued at 0000 UTC on 21 Jun 2018 and valid at 1200 UTC on 21 Jun 2018 for a) GEOS-5, b) NGAC, and c) CAMS NRT. Blue stars denote AERONET stations.

When aggregating the statistics by forecast lead time through the entire analysis period, GEOS-5 once again stands out as the best model of the three examined in this study, with the lowest FGE, ranging from 0.29–0.34 (Figure 5a) and near-zero MNMB of 0.01–0.05 (Figure 5b). CAMS was the next-best performing model, with an FGE of 0.40–0.42 and a clear positive bias (MNMB of 0.26–0.30). NGAC had the highest (worst) FGE of 0.55–0.56 for all five lead times, and a clear negative bias, with an MNMB ranging from -0.10 to -0.03 across the lead times. The general over-prediction of AOD_{550} by CAMS NRT and under-prediction by NGAC, paired with a neutral bias by GEOS-5, is consistent with results above. These results are also consistent with the statistics aggregated by model start hour, including for the 0600 and 1800 UTC cycles of GEOS-5 (not shown).

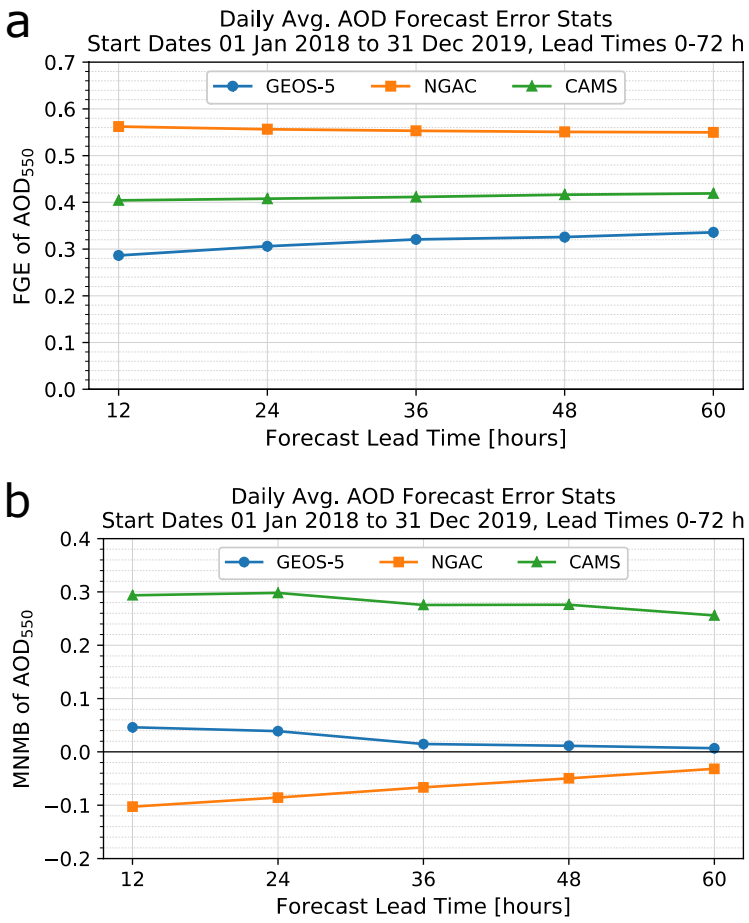

374

375 *Figure 5. a) Fractional gross error and b) modified normalized mean bias of daily average*
376 *AOD_{550} forecasts issued between 1 Jan 2018 and 31 Dec 2019 by the GEOS-5 (blue circles), NGAC*
377 *(orange squares), and CAMS NRT (green triangles) models, as a function of forecast lead time.*

378

379 In addition to the domain-average statistics examined so far, it is also useful to examine
380 model performance on a station-by-station basis. The correlation coefficients (R^2), for 00 UTC
381 day-1 forecasts (Figure 6a), day-2 forecasts (Figure 6b), and day-3 forecasts (Figure 6c) are
382 examined first. For all five start/lead time combinations (including the 1200 UTC day-2 and day-

383 3 lead times that are not shown), GEOS-5 has the highest R^2 value for most sites, with CAMS
384 having the highest R^2 for a few stations. NGAC has quite low R^2 values for all stations (all 0.26 or
385 lower), and is nearly uncorrelated with AERONET AOD_{550} observations at many stations. As
386 expected, correlations either stay constant or decline with increasing lead time. The median R^2
387 for GEOS-5 declines from 0.67 for 0000 UTC day-1 forecasts to 0.47 for day-3 forecasts. For
388 CAMS NRT the median R^2 declines from 0.53 to 0.47, while the NGAC median R^2 declines from
389 0.10 to 0.09 over the lead times examined here. From these plots and plots of FGE and MNMB
390 as a function of lead time, it can also be observed that the performance advantage for GEOS-5
391 over CAMS generally decreases somewhat with increasing lead time. It is also worth noting that
392 the very low R^2 values for the Tuz_Golu3 AERONET station at all lead times is largely due to the
393 small sample size of only 17 observations.

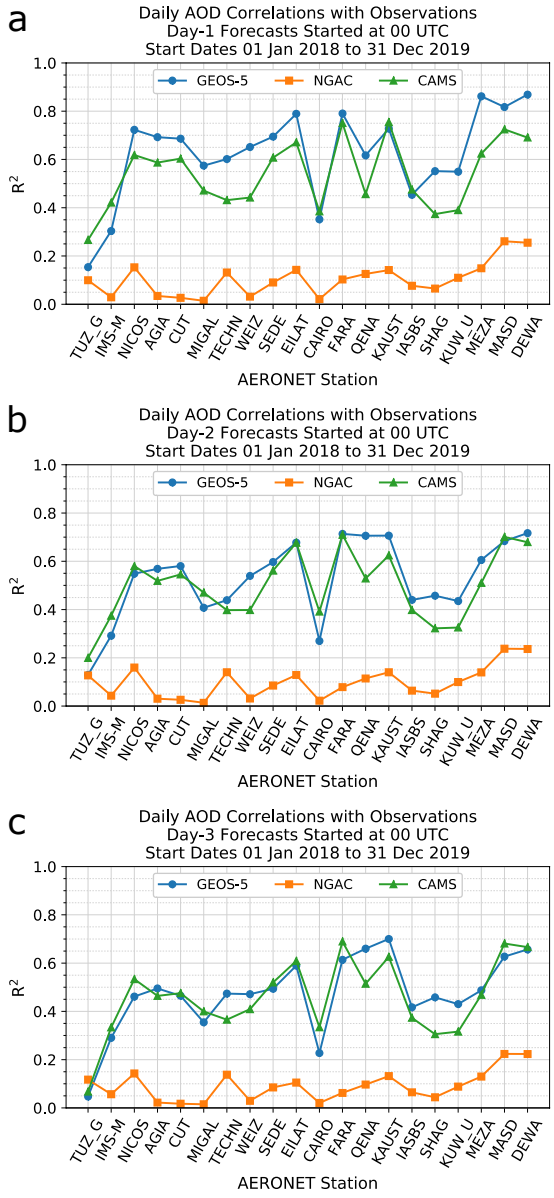

394

395 *Figure 6. Correlations of a) day-1, b) day-2, and c) day-3 daily-average AOD_{550} forecasts started*
396 *at 0000 UTC daily from 1 Jan 2018–31 Dec 2019 for the GEOS-5 (blue circles), NGAC (orange*
397 *squares), and CAMS NRT (green triangles) models against observations from the listed AERONET*
398 *stations.*

Looking at FGE and MNMB for each station individually in Figure 7a,b, once again, GEOS-5 performs the best at nearly all stations, with a median FGE of 0.30 and median MNMB of 0.03. There are two stations (Cairo_EMA_2 in Egypt and Migal in Israel) where CAMS NRT outperforms GEOS-5, but otherwise CAMS NRT is generally the second-best model, with a median FGE of 0.38 and median MNMB of 0.27. NGAC is the worst-performing model at most stations, with a median FGE of 0.57 and a median MNMB of -0.09. Once again, it is clear that CAMS NRT has substantial over-prediction of AOD_{550} in this region, while NGAC has consistent under-prediction of AOD and the largest absolute errors.

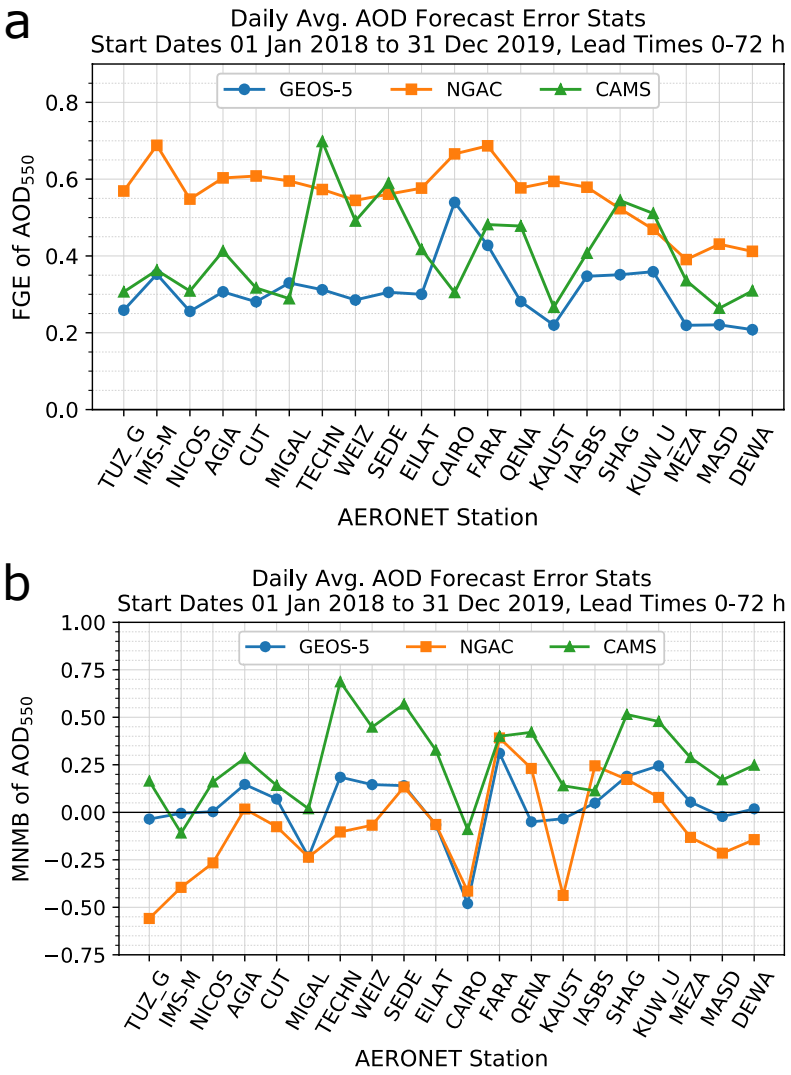

Figure 7. a) Fractional gross error and b) modified normalized mean bias for daily-average AOD_{550} forecasts issued from 1 Jan 2018–31 Dec 2019 for the GEOS-5 (blue circles), NGAC (orange squares), and CAMS NRT (green triangles) models against observations from the listed AERONET stations.

413 4.2 Dust storm prediction: Intensity and accuracy

414 Having looked at bulk model performance over the two-year period, now we briefly
415 examine model forecasts of AOD_{550} during two dust storm events in 2018 for which there are at
416 least partial AERONET observations.

417

418 *4.2.1 UAE's July 2018 dust storm*

419 During 28–31 July 2018 a severe, multi-day dust storm enveloped the southeastern
420 Arabian Peninsula, including the UAE, Oman, and portions of Saudi Arabia. The intense dust
421 storm, which was caused by cyclogenesis in the Empty Quarter Desert (also called Rub' al Khali,
422 in southeastern Saudi Arabia, bordering UAE and Oman), significantly impaired air quality
423 across the region, sharply curtailed solar irradiance, lofted dust to an altitude of 5 km, and
424 caused substantially warmer surface temperatures at night due to longwave emission of the
425 dust particles (Francis et al., 2021). Visible imagery from the MODIS instruments on NASA's
426 Terra and Aqua satellites from near mid-morning on 29 Jul 2018 and midday on 30 Jul 2018 in
427 Figure 8a,b, respectively, shows the large extent of the dust plume at the peak of the event,
428 with the center of circulation visible in the southeastern corner of Saudi Arabia, just south of
429 the UAE border.

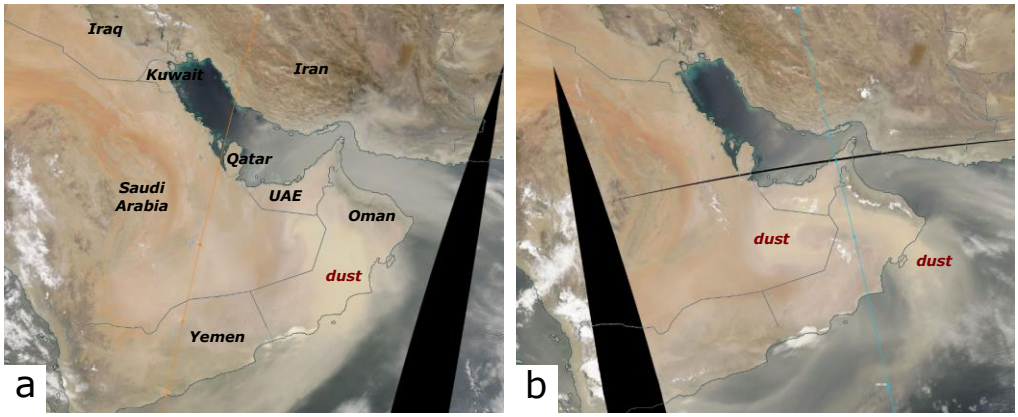

Figure 8. a) MODIS/Terra visible imagery on 29 Jul 2018 at 0725 UTC. The thin orange line is the Terra satellite overpass path (descending). b) MODIS/Aqua visible imagery on 30 Jul 2018 at 0938 UTC. The thin cyan line is the Aqua satellite overpass path (ascending). Images courtesy NASA Worldview.

Snapshots of the day-1 model forecasts of AOD_{550} for the three models are shown in Figure 9 and Figure 10, for the times closest to the MODIS images in Figure 8. Both GEOS-5 and CAMS indicate a significant dust storm event in the southeastern Arabian Peninsula, with total AOD_{550} values in the 3–5 range. The dust plume wrapped around the extratropical cyclone that is apparent in the MODIS imagery is present in the GEOS-5 and CAMS day-1 forecasts for 29 July 2018, and somewhat less so for forecasts on 30 July 2018, though the plume is still thick and expansive. Meanwhile, NGAC completely missed the event, even when initialized with the event already underway, with regional AOD_{550} values mostly under 0.5. This finding underlines the important benefit brought by the assimilation of spaceborne AOD observations in GEOS-5 and CAMS.

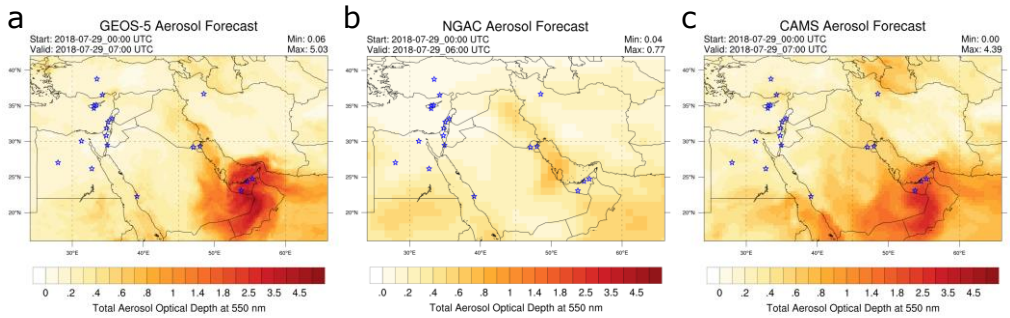

446

447 *Figure 9. Snapshot of AOD_{550} forecasts issued at 0000 UTC on 29 Jul 2018 and valid at 0700 UTC*
448 *on 29 Jun 2018 for a) GEOS-5, b) NGAC (valid time 0600 UTC), and c) CAMS NRT. Blue stars*
449 *denote AERONET stations. Compare with MODIS image in Figure 8a.*

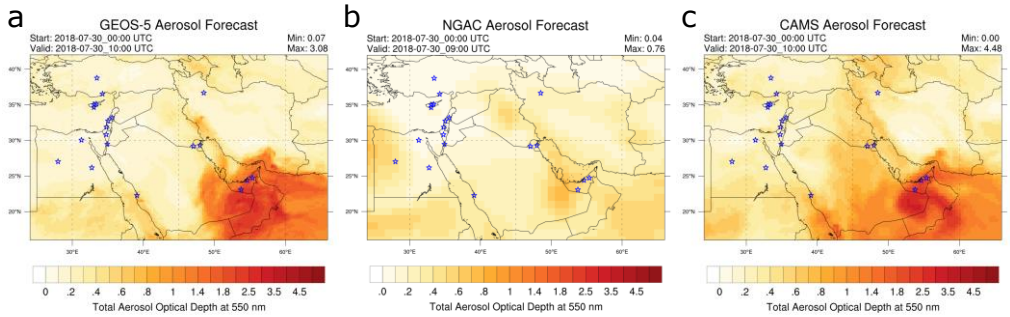

450

451 *Figure 10. Snapshot of AOD_{550} forecasts issued at 0000 UTC on 30 Jul 2018 and valid at 1000*
452 *UTC on 30 Jun 2018 for a) GEOS-5, b) NGAC (valid time 0900 UTC), and c) CAMS NRT. Blue stars*
453 *denote AERONET stations. Compare with MODIS image in Figure 8b.*

454

455 Corresponding time series of day-1, day-2, and day-3 daily average and hourly average
456 forecasts and observations at the Mezaira AERONET site in south-central UAE are presented in
457 Figure 11. (Neither of the other two AERONET stations in the UAE reported valid observations
458 during this event.) The Mezaira station did not report any valid observations on 30 July 2018 in
459 the L1.5 data, but did report for the other days during and surrounding this event. It is possible
460 that the AERONET cloud screening process (Giles et al., 2019; Smirnov et al., 2000) tends to

461 eliminate valid observations under dust-storm situations because their AOD is so high and
462 temporarily variable that they appear similar to a cloud signature. In fact, (Giles et al., 2019)
463 explicitly highlights potential problems with AERONET observations during dust storms: "The
464 Version 3 smoothness procedure could be affected by extreme changes in AOD due to
465 anomalous aerosol plumes (e.g., biomass burning or desert dust plumes)." Analysis of the Level
466 1 (raw, non-cloud filtered) data at Mezaira shows AOD_{550} values near or above 5.0 around 1000
467 and 1100 UTC on 29 July 2018, and then peaked at a remarkable 7.31 on 30 July 2018 at 0819
468 UTC (the lone observation that day); the L1.5 data are screened out during these times of
469 highest AOD in the L1 data (Table 2). If there were no clouds during this time period—and
470 visible satellite imagery on 29–30 July 2018 in Figure 8 indicates largely cloud-free skies across
471 the region—then the L1 AOD_{550} observations are presumptively accurate and were improperly
472 screened out. In any case, the proceeding analysis is with L1.5 data. Before and after the event,
473 the total AOD_{550} at Mezaira was typically in the 0.3–0.6 range. Through the day on 27 July, the
474 observed AOD rose to about 1.25; day-1 forecasts from GEOS-5 and NGAC tracked this increase
475 quite well. On both 28 and 29 July, all hourly-average observed AOD_{550} measurements were
476 above 3.0, and as high as 4.1. Over these two days, day-1 forecasts for GEOS-5 and CAMS were
477 both too low at most hours, though with predicted AOD_{550} ranging from 1.7–3.7 for GEOS-5 and
478 from 1.2–2.4 for CAMS NRT on these days. Overall, these two models successfully predicted the
479 existence of a severe dust storm, even if they underpredicted the severity. Unsurprisingly, day-
480 1 forecasts had the highest magnitudes and smallest biases, while day-2 and day-3 predicted
481 AOD_{550} was lower, but still suggestive of a potential dust storm at Mezaira. The NGAC day-1
482 predicted AOD_{550} consistently remained below 0.5 during 28–29 July, and below 0.6 on 30–31

July, totally missing the event at all lead times examined here. Such a severe forecast bust, which is not an uncommon event with NGAC in the Middle East, could be due partially to the coarse resolution of that model (1.0°x1.0°), or deficiencies in data assimilation or dust emission/source models, though a thorough analysis of the reasons is beyond the scope of this study.

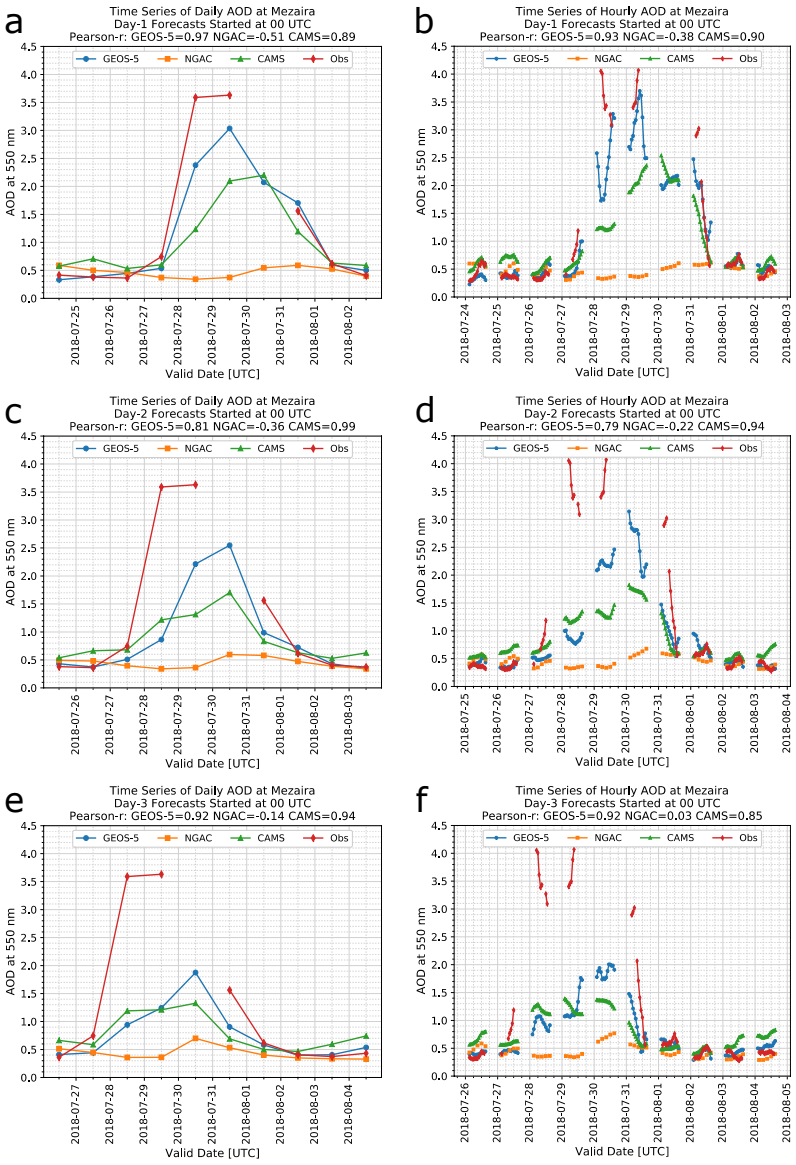

Figure 11. Time series of AOD_{550} for forecasts started at 0000 UTC daily from 24 Jul–2 Aug 2018 from the GEOS-5 (blue circles), NGAC (orange squares), and CAMS NRT (green triangles) models, and from L1.5 observations (red diamonds) at the Mezaira AERONET site in southern UAE. a) Day-1 daily average AOD; b) Day-1 hourly average AOD; c) Day-2 daily average AOD; d) Day-2 hourly average AOD; e) Day-3 daily average AOD; f) Day-3 hourly average AOD.

494

495 *Table 2. Time-centered hourly-average AOD_{550} observed values from the Mezaira AERONET*
496 *station during the middle three days (28–30 Jul 2018) of the dust storm in the UAE. Level 1 (raw)*
497 *and Level 1.5 (cloud-filtered) AOD_{550} values and numbers of observations in the hour are*
498 *included.*

Date/Time (UTC)	L1 AOD_{550}	L1.5 AOD_{550}	L1 n_{obs}	L1.5 n_{obs}
28 Jul 2018/0500	4.28	4.05	9	1
28 Jul 2018/0600	3.97	4.01	17	7
28 Jul 2018/0700	3.68	3.61	17	5
28 Jul 2018/0800	3.45	3.38	16	3
28 Jul 2018/0900	3.41	3.43	16	1
28 Jul 2018/1000	3.34	—	17	—
28 Jul 2018/1100	3.61	—	17	—
28 Jul 2018/1200	3.35	3.27	14	6
28 Jul 2018/1300	3.18	3.09	5	1
29 Jul 2018/0500	3.41	3.40	11	9
29 Jul 2018/0600	3.50	3.46	16	4
29 Jul 2018/0700	3.62	3.49	17	3
29 Jul 2018/0800	3.93	3.89	17	7
29 Jul 2018/0900	4.27	4.07	16	4
29 Jul 2018/1000	4.96	—	16	—
29 Jul 2018/1100	5.39	—	11	—
30 Jul 2018/0800	7.31	—	1	—

499

500 *4.2.2 Shagaya April 2018 dust storm*

501 On the afternoon of 26 April 2018, a dust storm was observed to move over the Shagaya
502 Renewable Energy Park (Al-Rasheedi et al., 2020) in western Kuwait. The haboob was
503 photographed moving over the Shagaya 50-MW concentrated solar power (CSP) plant at about
504 1130 UTC (1430 LST) that day (Figure 12). As the photograph shows, all the CSP collection
505 arrays were moved to a stowed position to protect the mirrors during the dust storm (the CSP
506 plant was also not yet operational at this time).

507

508 *Figure 12. Haboob moving over the Shagaya Renewable Energy Park in western Kuwait on 26*
509 *Apr 2018 at approximately 1130 UTC. Photo courtesy of EPC Company TSK. From Fig. 16 in (Al-*
510 *Rasheedi et al., 2020).*

511

512 Satellite imagery from MODIS/Aqua in Figure 13 indicates convection along a cold
513 frontal boundary attendant to a mature extratropical cyclone, with the line of convection still

about 100 km west of Kuwait at 1022 UTC, about four hours before the dust storm. The high wind associated with this convective frontal boundary is likely the direct cause of the haboob observed at Shagaya. Further evidence of a broad area of dust associated with frontal boundaries moving through the entire Fertile Crescent south into central Saudi Arabia is seen in the GEOS-5 and CAMS forecast AOD_{550} valid at 1400 UTC (Figure 14a,c), with AOD_{550} values generally in the 1.0–2.0 range in the area near and just west of Shagaya. As with the 28–31 July 2018 dust storm described in the previous subsection, the NGAC model completely missed the presence of the large-scale dust storm on this day, with AOD_{550} values only around 0.6 in the vicinity of western Kuwait (Figure 14b).

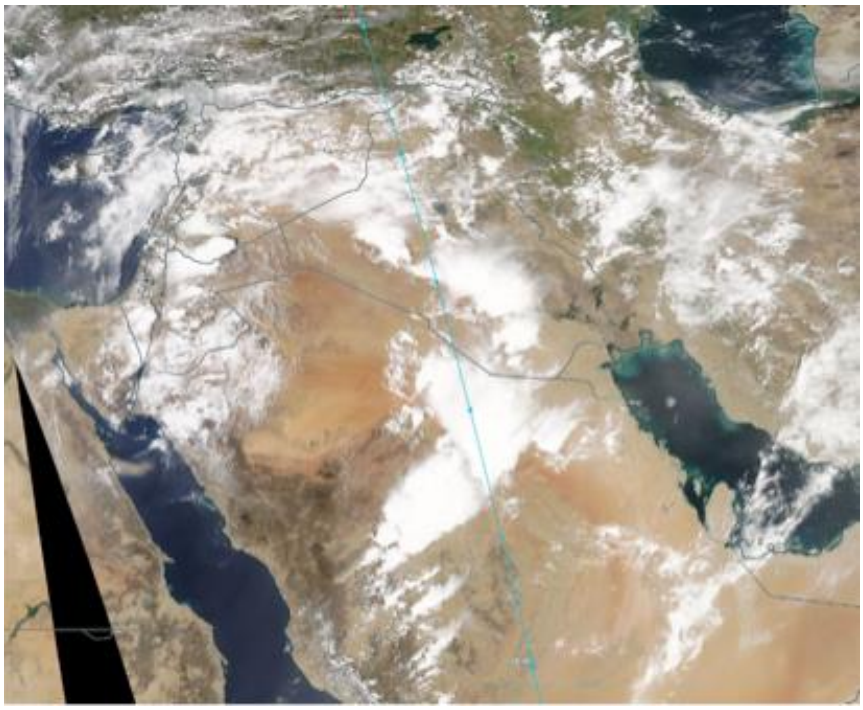

Figure 13. MODIS/Aqua visible imagery on 26 Apr 2018 at 1022 UTC. The thin cyan line is the Aqua satellite overpass path (ascending). Image courtesy NASA Worldview.

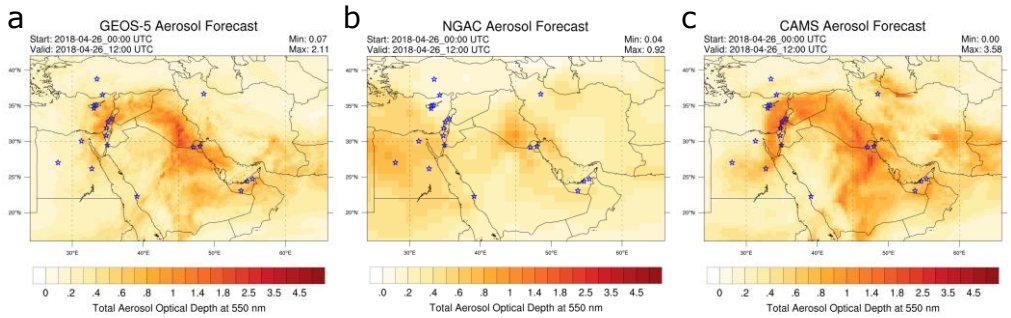

526

527 *Figure 14. Snapshot of AOD_{550} forecasts issued at 0000 UTC on 26 Apr 2018 and valid at 1200*
528 *UTC on 26 Apr 2018 for a) GEOS-5, b) NGAC, and c) CAMS NRT. Blue stars denote AERONET*
529 *stations. Compare with MODIS image in Figure 13.*

530

531 Examining time series of day-1 and day-2 AOD_{550} forecasts and observations for the
532 Shagaya_Park AERONET station (Figure 15), which is located just over 1 km away from the
533 location of the photograph in Figure 12, both GEOS-5 and CAMS NRT predict a dust storm that
534 day. Observed AOD_{550} increased from just below 0.4 in the morning to 0.6 at 1100 UTC, while
535 GEOS-5 remained about 0.4 higher during that time, as did CAMS NRT. Unfortunately, there are
536 no L1.5 AERONET hourly-average observations from Shagaya_Park after 1100 UTC this day. L1
537 (raw) AOD_{550} observations jumped from 0.84 to 3.29 to 3.82 from 1100 to 1200 to 1300 UTC,
538 respectively (Table 3), which is consistent with an expected sudden increase with the passage of
539 the haboob at about 1130 UTC. As mentioned above, it is possible that the observations that
540 afternoon during the dust storm were incorrectly screened out by the cloud filtering algorithm
541 of AERONET. (The Kuwait_University AERONET site in Kuwait City, about 100 km east of
542 Shagaya, did not report any valid L1.5 observations on this day, either.) While the AERONET
543 station did not record L1.5 measurements during the peak of the dust storm, we do see

evidence of the passage of the haboob from observations of global horizontal irradiance (GHI) at Shagaya initially dropping somewhat at 1055 UTC (coincident with L1 AOD_{550} observations jumping from about 0.59 at 1050 UTC to 0.90 at 1102 UTC), and then sharply dropping at about 1130 UTC in Figure 16 (coincident with L1 AOD_{550} observations markedly increasing from 1.13 at 1129 UTC to 1.75 at 1132 UTC, and then to 3.11 at 1141 UTC, before peaking at 4.36 at 1217 UTC). From both the 1200 UTC map and the forecast model time series of AOD_{550}, GEOS-5 predicted AOD somewhat too slow and too weak for this event, with AOD_{550} rising only from 1.0 to 1.3 from 1200–1500 UTC. CAMS NRT brought two waves of dust through Shagaya before the photographed event, one in the morning (0500 UTC) and a second wave in early afternoon, around 1100 UTC, increasing AOD_{550} to about 1.1 by 1500 UTC. Hence, it was still too weak compared to L1 observations at Shagaya, though the forecast map at 1200 UTC (Figure 14) indicates good timing for the event, but with a small displacement error, with the peak of the dust storm being just over the border into Saudi Arabia. Day-2 and day-3 forecasts valid on 26 April 2018 (Figure 15c-f) did show AOD_{550} values near and above 1.0 for both GEOS-5 and CAMS NRT, with CAMS NRT indicating a potentially significant dust storm on day-2 and day-3, though still an underestimate of the L1 AOD_{550} observations at the Shagaya_Park AERONET station.

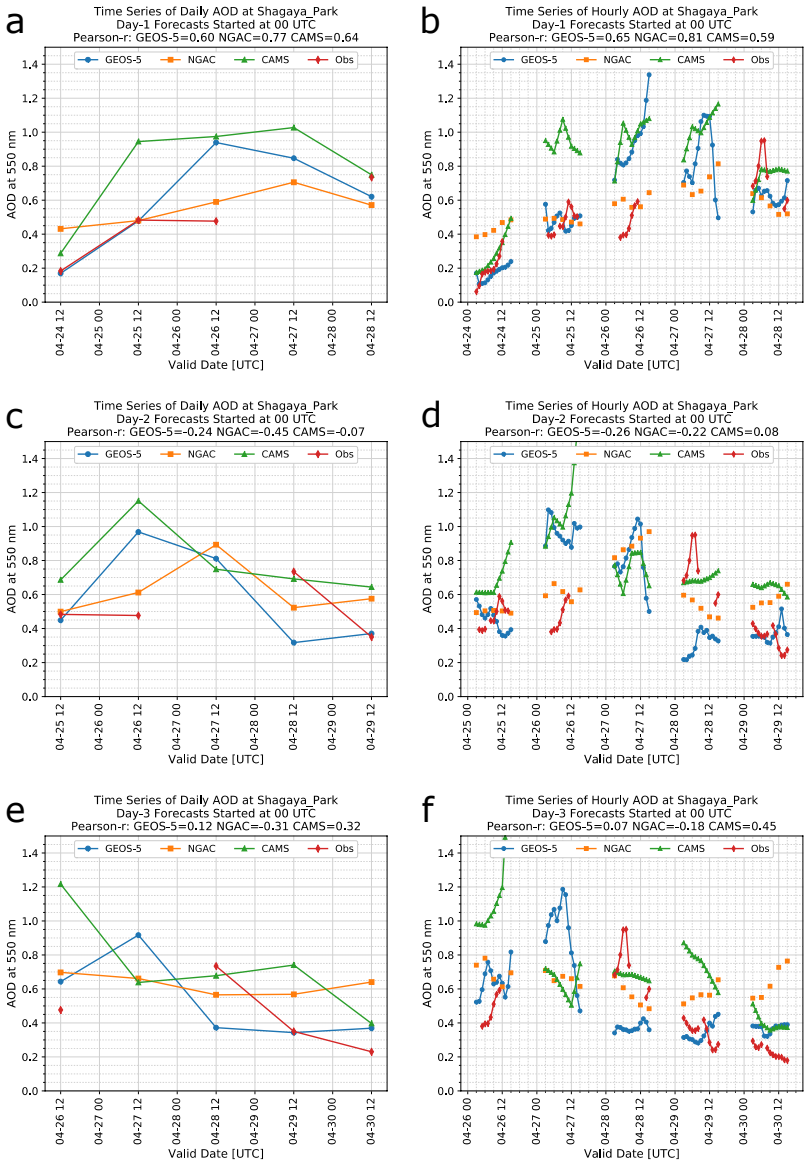

560

561 *Figure 15. Time series of AOD_{550} for forecasts started at 0000 UTC daily from 24–28 Apr 2018*
562 *from the GEOS-5 (blue circles), NGAC (orange squares), and CAMS NRT (green triangles) models,*
563 *and from observations (red diamonds) at the Shagaya_Park AERONET site in western Kuwait. a)*
564 *Day-1 daily average AOD; b) Day-1 hourly average AOD; c) Day-2 daily average AOD; d) Day-2*
565 *hourly average AOD; e) Day-3 daily average AOD; and f) Day-3 hourly average AOD.*

Table 3. Time-centered hourly-average AOD_{550} observed values from the Shagaya_Park AERONET station on 26 Apr 2018, the day of the dust storm at Shagaya. Level 1 (raw) and Level 1.5 (cloud-filtered) AOD_{550} values and numbers of observations in the hour are included.

Date/Time (UTC)	**L1 AOD_{550}**	**L1.5 AOD_{550}**	**L1 n_{obs}**	**L1.5 n_{obs}**
26 Apr 2018/0400	0.49	—	3	—
26 Apr 2018/0500	0.46	0.38	5	1
26 Apr 2018/0600	0.41	0.40	14	10
26 Apr 2018/0700	0.40	0.40	17	16
26 Apr 2018/0800	0.43	0.43	17	16
26 Apr 2018/0900	0.52	0.51	16	12
26 Apr 2018/1000	0.57	0.57	17	17
26 Apr 2018/1100	0.84	0.59	16	6
26 Apr 2018/1200	3.29	—	10	—
26 Apr 2018/1300	3.82	—	1	—

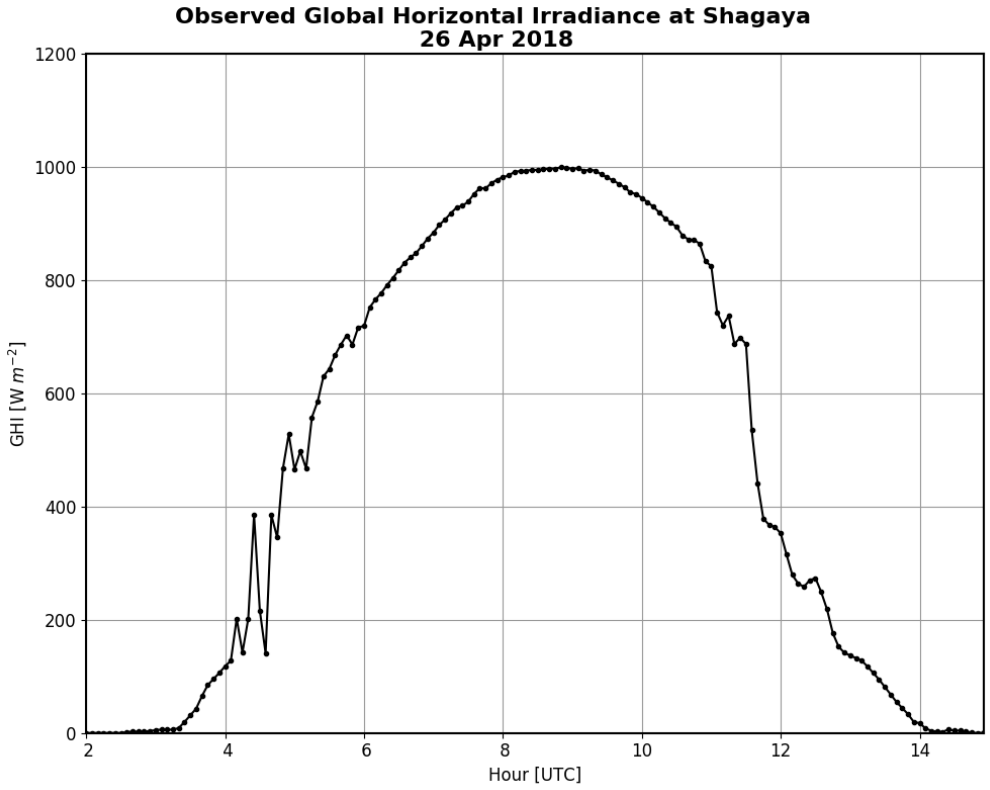

Figure 16. Time series of GHI observations on 26 Apr 2018 from a pyranometer located at the Shagaya Renewable Energy Park, about 1 km from the Shagaya_Park AERONET station. The haboob was photographed moving over Shagaya at approximately 1130 UTC, coinciding with a steep drop in GHI. Plot courtesy of Julia Pearson (NCAR).

4.3 Potential impacts on solar energy production

High-AOD events such as the two dust storms discussed above cause a substantial reduction in solar energy generation, by reducing the solar irradiance that reaches the collectors or panels and by creating intense soiling (Al-Rasheedi et al., 2020). This effect is much sharper for CSP plants, such as the one pictured at Shagaya in Figure 12, as they convert direct

582 normal irradiance (DNI) to power. Any scattering or absorption of radiation by dust particles,
583 other aerosols, or clouds, will noticeably or completely attenuate DNI at the surface. Dust
584 storms can also cause problems for CSP installations because their mirrors must be secured
585 ahead of time in a stowed position. Unfortunately, there were no DNI observations at Shagaya
586 during this event, as the CSP plant was still under construction and not yet operational.
587 Photovoltaic (PV) solar plants convert GHI to power. Because GHI includes contributions from
588 diffuse radiation, GHI is attenuated less than DNI is by the presence of aerosols, but PV power
589 production can still be noticeably reduced by heavy aerosol loading and soiling.
590 Accurate forecasting of GHI and DNI in cloudless conditions requires accurate
591 forecasting of total AOD_{550} and dust storms. Particularly in desert or other arid regions where
592 clear skies predominate, such as the Middle East, good irradiance forecasts are a crucial
593 component for accurate solar power forecasts, which are necessary for effective grid
594 management and to optimize the cleaning cycle of collectors or mirrors (especially considering
595 the lack of water in the area).
596 The results presented in this paper, with GEOS-5 AOD_{550} forecasts performing better
597 than those from CAMS NRT or NGAC in the Middle East over a two-year period, indicates that
598 coupling GEOS-5 AOD_{550} forecasts with high-resolution forecast models, such as the Weather
599 Research and Forecasting (WRF) model (Powers et al., 2017) configured for solar forecasting
600 applications (WRF-Solar®) (Jiménez, Alessandrini, et al., 2016; Jiménez, Hacker, et al., 2016),
601 could yield improved GHI and DNI forecasts. This is an area of active ongoing research, including
602 for solar power forecasting in Kuwait (Haupt et al., 2020), and irradiance forecasting in Arizona,
603 where (Bunn et al., 2020) found that GEOS-5 AOD_{550} forecasts coupled with WRF provided

604 significantly improved GHI forecasts compared to other methods. This finding builds off of
605 (Jiménez, Hacker, et al., 2016), which found that WRF-Solar with GEOS-5 AOD_{550} forecasts
606 imposed results in reduced GHI and DNI errors during clear-sky conditions for a network of
607 high-quality irradiance sensors in the U.S., compared to either imposing no aerosol information
608 or imposing AOD from various aerosol climatologies. Furthermore, recent analysis of the 10-
609 MW wind plant at Shagaya also demonstrates the detrimental effects of dust accumulation on
610 wind power production in the summer (Al-Rasheedi et al. 2021a,b, manuscripts submitted to
611 *Sustainable Energy Technologies and Assessments*), indicating that good dust forecasting in this
612 region would be beneficial to wind plant operators in desert environments as well, not just
613 solar plant operators.
614

615 **5. Conclusion**

616 In this study we examined model forecasts of aerosol optical depth at 550 nm (AOD_{550})
617 in the Middle East issued over a two-year time period, 2018–2019. The forecasts we compared
618 here are 1–3-day forecasts from 0000 and 1200 UTC cycles of operational models from three
619 major forecasting centers: GEOS-5 from NASA, NGAC from NOAA, and CAMS NRT from ECMWF.
620 We processed the AOD_{550} forecasts to daily averages to match the standard AOD_{550}
621 observations produced by a network of 20 AERONET stations across the Middle East.

622 We validated forecasts using a suite of standard metrics, focusing on fractional gross
623 error (FGE), modified normalized mean bias (MNMB), and correlation (R^2). We stratified our
624 results by AERONET station, by forecast lead time, and by model start date/time. A few
625 consistent conclusions emerged:

1) GEOS-5 forecasts generally had the lowest (best) FGE and near-zero MNMB (an MNMB of 0 is perfect), and the highest R^2 through most forecast start dates/times, lead times, and for all but two of the 20 AERONET stations;
2) CAMS NRT forecasts had the second-best FGE and a generally positive MNMB, indicating a general over-prediction of total AOD_{550} (much of which in this region comes from dust), and R^2 values only slightly lower than GEOS-5; at the two AERONET sites where GEOS-5 was not the best-performing model, CAMS NRT was the best-performing model on average;
3) NGAC forecasts had the worst FGE, and a generally negative MNMB, indicating a general under-prediction of total AOD_{550} throughout 2018–2019 in the Middle East, along with very low R^2 values, indicating a general lack of forecast skill for even trends in AOD_{550};
4) Forecast accuracy generally declined with increasing lead time, as expected.

It should perhaps not be surprising that GEOS-5 was found to be the best performing model in this region, given that NASA assimilates aerosol measurements from satellites and calibrates that data against AERONET stations globally. Similarly, it was not unexpected that NGAC would perform worse than GEOS-5 or CAMS NRT, as NGAC runs on a significantly coarser model grid. Furthermore, NGAC v2, while it uses the same aerosol module and emissions as GEOS-5, does not assimilate satellite AOD retrievals or calibrate its AOD predictions against AERONET, unlike GEOS-5. It can be concluded that such processes are likely essential to obtain good AOD forecasts.

We also examined model forecast performance during two dust storm events—a four-day severe dust storm in the UAE and Empty Quarter Desert during 28–31 July 2018, and a dust storm in Kuwait on 26 April 2018. For these two events, we examined hourly-average forecasts and L1.5 (cloud-screened) AERONET observations, and found similar conclusions to those mentioned above, with GEOS-5 and CAMS NRT qualitatively performing reasonably well on timing and magnitude, and NGAC completely missing these large-scale dust storms. Unfortunately, the AERONET stations did not report L1.5 data during the peak of these dust storm events, thus limiting the ability to fully validate the three forecast models. Fortunately, L1 (raw) AERONET data was available for some additional hours during these two events, indicating peak instantaneous AOD_{550} values of 7.31 in the UAE dust storm and 4.36 in the Kuwait dust storm. Visible satellite imagery from MODIS indicates there was likely no cloud cover obscuring the AERONET stations at these times, which strongly suggests that these raw data were incorrectly filtered out by the current cloud-screening algorithms applied to process AERONET data from L1 to L1.5. Additional research should be conducted to attempt to ameliorate this complex issue of cloud filtering in AERONET observational data.

Forecasts of dust storms and overall aerosol loading are relevant for several fields, most notably air quality forecasting, solar energy forecasting, and cloud microphysics. Future research will seek to further refine and improve AOD_{550} forecasting for these applications using high-resolution modeling, such as with the WRF model.

Acknowledgements

Funding for this project was supplied by the Kuwait Institute for Scientific Research (KISR) under contract number P-KISR-12, with Dr. Majed Al-Rasheedi of KISR serving as Project Monitor. This material is based upon work performed by the National Center for Atmospheric Research, which is a major facility sponsored by the National Science Foundation under Cooperative Agreement No. 1852977. The Principal Investigator and staff of each of the 20 AERONET stations used in this investigation are warmly thanked for establishing and maintaining this invaluable source of data. This publication contains modified Copernicus Atmosphere Monitoring Service Information [2018–2019], and neither the European Commission nor ECMWF is responsible for any use that may be made of the information it contains. The authors also thank Sue Ellen Haupt and Branko Kosović of NCAR for helpful comments on the manuscript.

Data Availability Statement

All data supporting this research are stored in a public repository (Lee et al., 2021) at https://dashrepo.ucar.edu/dataset/187_jaredlee.html for at least the next five years.

References

Al-Rasheedi, M., M. Al-Khayat, C. A. Gueymard, S. E. Haupt, B. Kosović, and J. A. Lee, 2021a: Analysis of a 10-MW wind farm at the Shagaya Renewable Energy Park in the hot, dusty

environment of Kuwait. Part 1: Performance evaluation of the wind power to energy generation. *Sustain. Energy Tech. Assess.*, submitted.

Al-Rasheedi, M. M. Al-Khayat, C. A. Gueymard, S. E. Haupt, B. Kosović, and J. A. Lee, 2021b: Analysis of a 10-MW wind farm at the Shagaya Renewable Energy Park in the hot, dusty environment of Kuwait. Part 2: Combined dust and high-temperature effects on the performance of wind turbines. *Sustain. Energy Tech. Assess.*, submitted.

Ahmady-Birgani, H., McQueen, K. G., & Mirnejad, H. (2018). Characteristics of mineral dust impacting the Persian Gulf. *Aeolian Research*, *30*, 11–19. https://doi.org/10.1016/j.aeolia.2017.11.001

Alam, K., Trautmann, T., Blaschke, T., & Subhan, F. (2014). Changes in aerosol optical properties due to dust storms in the Middle East and Southwest Asia. *Remote Sensing of Environment*, *143*, 216–227. https://doi.org/10.1016/j.rse.2013.12.021

Al-Hemoud, A., Al-Dousari, A., Al-Shatti, A., Al-Khayat, A., Behbehani, W., & Malak, M. (2018). Health Impact Assessment Associated with Exposure to PM10 and Dust Storms in Kuwait. *Atmosphere*, *9*(1), 6. https://doi.org/10.3390/atmos9010006

Al-Hemoud, A., Al-Dousari, A., Misak, R., Al-Sudairawi, M., Naseeb, A., Al-Dashti, H., & Al-Dousari, N. (2019). Economic Impact and Risk Assessment of Sand and Dust Storms (SDS) on the Oil and Gas Industry in Kuwait. *Sustainability*, *11*(1), 200. https://doi.org/10.3390/su11010200

Alizadeh-Choobari, O., Ghafarian, P., & Owlad, E. (2016). Temporal variations in the frequency and concentration of dust events over Iran based on surface observations. *International Journal of Climatology*, *36*(4), 2050–2062. https://doi.org/10.1002/joc.4479

710 Alnaser, N. W., & Alnaser, W. E. (2019). The impact of the rise of using solar energy in GCC
711 countries. *Renewable Energy and Environmental Sustainability*, *4*, 7.
712 https://doi.org/10.1051/rees/2019004
713 Al-Rasheedi, M., Gueymard, C. A., Al-Khayat, M., Ismail, A., Lee, J. A., & Al-Duaj, H. (2020).
714 Performance evaluation of a utility-scale dual-technology photovoltaic power plant at
715 the Shagaya Renewable Energy Park in Kuwait. *Renewable and Sustainable Energy*
716 *Reviews*, *133*, 110139. https://doi.org/10.1016/j.rser.2020.110139
717 Alsayegh, O., Saker, N., & Alqattan, A. (2018). Integrating sustainable energy strategy with the
718 second development plan of Kuwait. *Renewable and Sustainable Energy Reviews*, *82*,
719 3430–3440. https://doi.org/10.1016/j.rser.2017.10.048
720 Arkian, F. (2017). Short-Term Variations of Aerosol Optical Depth during the Severe Dust Storm
721 in 2015 over the Middle East and Long-term Variations of Aerosol Optical Properties.
722 *Environment Pollution and Climate Change*, *1*(3), 1–11. https://doi.org/10.4172/2573-
723 458X.1000127
724 Bangalath, H. K., & Stenchikov, G. (2016). Sensitivity of the Middle East–North African Tropical
725 Rainbelt to Dust Shortwave Absorption: A High-Resolution AGCM Experiment. *Journal of*
726 *Climate*, *29*(19), 7103–7126. https://doi.org/10.1175/JCLI-D-15-0827.1
727 Basart, S., Pérez, C., Nickovic, S., Cuevas, E., & Baldasano, J. (2012). Development and
728 evaluation of the BSC-DREAM8b dust regional model over Northern Africa, the
729 Mediterranean and the Middle East. *Tellus B: Chemical and Physical Meteorology*, *64*(1),
730 18539. https://doi.org/10.3402/tellusb.v64i0.18539

731 Basha, G., Phanikumar, D. V., Kumar, K. N., Ouarda, T. B. M. J., & Marpu, P. R. (2015).
732 Investigation of aerosol optical, physical, and radiative characteristics of a severe dust
733 storm observed over UAE. *Remote Sensing of Environment*, *169*, 404–417.
734 https://doi.org/10.1016/j.rse.2015.08.033
735 Beegum, S. N., Gherboudj, I., Chaouch, N., Temimi, M., & Ghedira, H. (2018). Simulation and
736 analysis of synoptic scale dust storms over the Arabian Peninsula. *Atmospheric*
737 *Research*, *199*, 62–81. https://doi.org/10.1016/j.atmosres.2017.09.003
738 Benedetti, A., Morcrette, J.-J., Boucher, O., Dethof, A., Engelen, R. J., Fisher, M., et al. (2009).
739 Aerosol analysis and forecast in the European Centre for Medium-Range Weather
740 Forecasts Integrated Forecast System: 2. Data assimilation. *Journal of Geophysical*
741 *Research: Atmospheres*, *114*(D13). https://doi.org/10.1029/2008JD011115
742 Benedetti, A., Baldasano, J. M., Basart, S., Benincasa, F., Boucher, O., Brooks, M. E., et al.
743 (2014). Operational Dust Prediction. In P. Knippertz & J.-B. W. Stuut (Eds.), *Mineral Dust:*
744 *A Key Player in the Earth System* (pp. 223–265). Dordrecht: Springer Netherlands.
745 https://doi.org/10.1007/978-94-017-8978-3_10
746 Benedetti, A., Giuseppe, F. D., Jones, L., Peuch, V.-H., Rémy, S., & Zhang, X. (2019). The value of
747 satellite observations in the analysis and short-range prediction of Asian dust.
748 *Atmospheric Chemistry and Physics*, *19*(2), 987–998. https://doi.org/10.5194/acp-19-
749 987-2019
750 Benedetti, A., Di Giuseppe, F., Jones, L., Peuch, V.-H., Rémy, S., & Zhang, X. (2019). The value of
751 satellite observations in the analysis and short-range prediction of Asian dust.

Atmospheric Chemistry and Physics, *19*(2), 987–998. https://doi.org/10.5194/acp-19-987-2019

Buchard, V., Silva, A. M. da, Colarco, P. R., Darmenov, A., Randles, C. A., Govindaraju, R., et al. (2015). Using the OMI aerosol index and absorption aerosol optical depth to evaluate the NASA MERRA Aerosol Reanalysis. *Atmospheric Chemistry and Physics*, *15*(10), 5743–5760. https://doi.org/10.5194/acp-15-5743-2015

Bunn, P. T. W., Holmgren, W. F., Leuthold, M., & Castro, C. L. (2020). Using GEOS-5 forecast products to represent aerosol optical depth in operational day-ahead solar irradiance forecasts for the southwest United States. *Journal of Renewable and Sustainable Energy*, *12*(5), 053702. https://doi.org/10.1063/5.0020785

Calastrini, F., Guarnieri, F., Becagli, S., Busillo, C., Chiari, M., Dayan, U., et al. (2012, September 16). Desert Dust Outbreaks over Mediterranean Basin: A Modeling, Observational, and Synoptic Analysis Approach [Research Article]. https://doi.org/10.1155/2012/246874

Chin, M., Ginoux, P., Kinne, S., Torres, O., Holben, B. N., Duncan, B. N., et al. (2002). Tropospheric Aerosol Optical Thickness from the GOCART Model and Comparisons with Satellite and Sun Photometer Measurements. *Journal of the Atmospheric Sciences*, *59*(3), 461–483. https://doi.org/10.1175/1520-0469(2002)059<0461:TAOTFT>2.0.CO;2

Choobari, O. A., Zawar-Reza, P., & Sturman, A. (2014). The global distribution of mineral dust and its impacts on the climate system: A review. *Atmospheric Research*, *138*, 152–165. https://doi.org/10.1016/j.atmosres.2013.11.007

Colarco, P. R., Silva, A. da, Chin, M., & Diehl, T. (2010). Online simulations of global aerosol distributions in the NASA GEOS-4 model and comparisons to satellite and ground-based

774 aerosol optical depth. *Journal of Geophysical Research: Atmospheres*, *115*(D14).
775 https://doi.org/10.1029/2009JD012820
776 Colarco, P. R., Nowottnick, E. P., Randles, C. A., Yi, B., Yang, P., Kim, K.-M., et al. (2014). Impact
777 of radiatively interactive dust aerosols in the NASA GEOS-5 climate model: Sensitivity to
778 dust particle shape and refractive index. *Journal of Geophysical Research: Atmospheres*,
779 *119*(2), 753–786. https://doi.org/10.1002/2013JD020046
780 Copernicus. (2020, February 19). CAMS Near-real-time Global analysis and forecast daily data
781 [Text]. Retrieved August 3, 2020, from
782 https://www.ecmwf.int/en/forecasts/dataset/cams-near-real-time-global-analysis-and-
783 forecast-daily-data
784 ECMWF. (2019). Operational configurations of the ECMWF Integrated Forecasting System (IFS)
785 [Text]. Retrieved August 3, 2020, from
786 https://www.ecmwf.int/en/forecasts/documentation-and-support
787 Eissa, Y., Naseema Beegum, S., Gherboudj, I., Chaouch, N., Al Sudairi, J., Jones, R. K., et al.
788 (2018). Prediction of the day-ahead clear-sky downwelling surface solar irradiances
789 using the REST2 model and WRF-CHIMERE simulations over the Arabian Peninsula. *Solar*
790 *Energy*, *162*, 36–44. https://doi.org/10.1016/j.solener.2018.01.003
791 Engelen, R. (2019, July 5). Implementation of IFS cycle 46r1 - Copernicus Services. Retrieved
792 August 3, 2020, from
793 https://confluence.ecmwf.int/display/COPSRV/Implementation+of+IFS+cycle+46r1

794 Filip, L., & Stefan, S. (2011). Study of the correlation between the near-ground PM10 mass
795 concentration and the aerosol optical depth. *Journal of Atmospheric and Solar-*
796 *Terrestrial Physics*, *73*(13), 1883–1889. https://doi.org/10.1016/j.jastp.2011.04.027
797 Flemming, J., Huijnen, V., Arteta, J., Bechtold, P., Beljaars, A., Blechschmidt, A.-M., et al. (2015).
798 Tropospheric chemistry in the Integrated Forecasting System of ECMWF. *Geoscientific*
799 *Model Development*, *8*(4), 975–1003. https://doi.org/10.5194/gmd-8-975-2015
800 Francis, D., Chaboureau, J.-P., Nelli, N., Cuesta, J., Alshamsi, N., Temimi, M., et al. (2021).
801 Summertime dust storms over the Arabian Peninsula and impacts on radiation,
802 circulation, cloud development and rain. *Atmospheric Research*, *250*, 105364.
803 https://doi.org/10.1016/j.atmosres.2020.105364
804 Giles, D. M., Sinyuk, A., Sorokin, M. G., Schafer, J. S., Smirnov, A., Slutsker, I., et al. (2019).
805 Advancements in the Aerosol Robotic Network (AERONET) Version 3 database –
806 automated near-real-time quality control algorithm with improved cloud screening for
807 Sun photometer aerosol optical depth (AOD) measurements. *Atmospheric Measurement*
808 *Techniques*, *12*(1), 169–209. https://doi.org/10.5194/amt-12-169-2019
809 Ginoux, P., Chin, M., Tegen, I., Prospero, J. M., Holben, B., Dubovik, O., & Lin, S.-J. (2001).
810 Sources and distributions of dust aerosols simulated with the GOCART model. *Journal of*
811 *Geophysical Research: Atmospheres*, *106*(D17), 20255–20273.
812 https://doi.org/10.1029/2000JD000053
813 Hamidi, M., Kavianpour, M. R., & Shao, Y. (2017). A quantitative evaluation of the 3–8 July 2009
814 Shamal dust storm. *Aeolian Research*, *24*, 133–143.
815 https://doi.org/10.1016/j.aeolia.2016.12.004

816 Haupt, S. E., McCandless, T. C., Dettling, S., Alessandrini, S., Lee, J. A., Linden, S., et al. (2020).
817 Combining Artificial Intelligence with Physics-based Methods for Probabilistic
818 Renewable Energy Forecasting. *Energies*, *13*(8), 1979.
819 https://doi.org/10.3390/en13081979
820 Haustein, K., Pérez, C., Baldasano, J. M., Jorba, O., Basart, S., Miller, R. L., et al. (2012).
821 Atmospheric dust modeling from meso to global scales with the online NMMB/BSC-Dust
822 model – Part 2: Experimental campaigns in Northern Africa. *Atmospheric Chemistry and*
823 *Physics*, *12*(6), 2933–2958. https://doi.org/10.5194/acp-12-2933-2012
824 Haywood, J., Francis, P., Osborne, S., Glew, M., Loeb, N., Highwood, E., et al. (2003). Radiative
825 properties and direct radiative effect of Saharan dust measured by the C-130 aircraft
826 during SHADE: 1. Solar spectrum. *Journal of Geophysical Research: Atmospheres*,
827 *108*(D18). https://doi.org/10.1029/2002JD002687
828 Holben, B. N., Eck, T. F., Slutsker, I., Tanré, D., Buis, J. P., Setzer, A., et al. (1998). AERONET—A
829 Federated Instrument Network and Data Archive for Aerosol Characterization. *Remote*
830 *Sensing of Environment*, *66*(1), 1–16. https://doi.org/10.1016/S0034-4257(98)00031-5
831 Hsu, N. C., Gautam, R., Sayer, A. M., Bettenhausen, C., Li, C., Jeong, M. J., et al. (2012). Global
832 and regional trends of aerosol optical depth over land and ocean using SeaWiFS
833 measurements from 1997 to 2010. *Atmospheric Chemistry and Physics*, *12*(17), 8037–
834 8053. https://doi.org/10.5194/acp-12-8037-2012
835 Huang, J., Wang, T., Wang, W., Li, Z., & Yan, H. (2014). Climate effects of dust aerosols over East
836 Asian arid and semiarid regions. *Journal of Geophysical Research: Atmospheres*, *119*(19),
837 11,398-11,416. https://doi.org/10.1002/2014JD021796

838 Huijnen, V., Williams, J., Weele, M. van, Noije, T. van, Krol, M., Dentener, F., et al. (2010). The
839 global chemistry transport model TM5: description and evaluation of the tropospheric
840 chemistry version 3.0. *Geoscientific Model Development*, *3*(2), 445–473.
841 https://doi.org/10.5194/gmd-3-445-2010
842 Huneeus, N., Schulz, M., Balkanski, Y., Griesfeller, J., Prospero, J., Kinne, S., et al. (2011). Global
843 dust model intercomparison in AeroCom phase I. *Atmospheric Chemistry and Physics*,
844 *11*(15), 7781–7816. https://doi.org/10.5194/acp-11-7781-2011
845 Huneeus, N., Basart, S., Fiedler, S., Morcrette, J.-J., Benedetti, A., Mulcahy, J., et al. (2016).
846 Forecasting the northern African dust outbreak towards Europe in April 2011: a model
847 intercomparison. *Atmospheric Chemistry and Physics*, *16*(8), 4967–4986.
848 https://doi.org/10.5194/acp-16-4967-2016
849 Husar, R. B., Tratt, D. M., Schichtel, B. A., Falke, S. R., Li, F., Jaffe, D., et al. (2001). Asian dust
850 events of April 1998. *Journal of Geophysical Research: Atmospheres*, *106*(D16), 18317–
851 18330. https://doi.org/10.1029/2000JD900788
852 Inness, A., Ades, M., Agustí-Panareda, A., Barré, J., Benedictow, A., Blechschmidt, A.-M., et al.
853 (2019). The CAMS reanalysis of atmospheric composition. *Atmospheric Chemistry and*
854 *Physics*, *19*(6), 3515–3556. https://doi.org/10.5194/acp-19-3515-2019
855 IPCC. (2013). *Climate Change 2013: The Physical Science Basis. Contribution of Working Group I*
856 *to the Fifth Assessment Report of the Intergovernmental Panel on Climate Change*
857 *[Stocker, T.F., D. Qin, G.-K. Plattner, M. Tignor, S.K. Allen, J. Boschung, A. Nauels, Y. Xia,*
858 *V. Bex and P.M. Midgley (eds.)]*. Cambridge University Press, Cambridge, United

Kingdom and New York, NY, USA, 1585 pp. Retrieved from https://www.ipcc.ch/report/ar5/wg1/

Jiménez, P. A., Alessandrini, S., Haupt, S. E., Deng, A., Kosovic, B., Lee, J. A., & Delle Monache, L. (2016). The Role of Unresolved Clouds on Short-Range Global Horizontal Irradiance Predictability. *Monthly Weather Review*, *144*(9), 3099–3107. https://doi.org/10.1175/MWR-D-16-0104.1

Jiménez, P. A., Hacker, J. P., Dudhia, J., Haupt, S. E., Ruiz-Arias, J. A., Gueymard, C. A., et al. (2016). WRF-Solar: Description and Clear-Sky Assessment of an Augmented NWP Model for Solar Power Prediction. *Bulletin of the American Meteorological Society*, *97*(7), 1249–1264. https://doi.org/10.1175/BAMS-D-14-00279.1

Jin, Q., Wei, J., & Yang, Z.-L. (2014). Positive response of Indian summer rainfall to Middle East dust. *Geophysical Research Letters*, *41*(11), 4068–4074. https://doi.org/10.1002/2014GL059980

Karagulian, F., Temimi, M., Ghebreyesus, D., Weston, M., Kondapalli, N. K., Valappil, V. K., et al. (2019). Analysis of a severe dust storm and its impact on air quality conditions using WRF-Chem modeling, satellite imagery, and ground observations. *Air Quality, Atmosphere & Health*, *12*(4), 453–470. https://doi.org/10.1007/s11869-019-00674-z

Kaufman, Y. J., Koren, I., Remer, L. A., Tanré, D., Ginoux, P., & Fan, S. (2005). Dust transport and deposition observed from the Terra-Moderate Resolution Imaging Spectroradiometer (MODIS) spacecraft over the Atlantic Ocean. *Journal of Geophysical Research: Atmospheres*, *110*(D10). https://doi.org/10.1029/2003JD004436

880 Kim, D., Chin, M., Yu, H., Diehl, T., Tan, Q., Kahn, R. A., et al. (2014). Sources, sinks, and
881 transatlantic transport of North African dust aerosol: A multimodel analysis and
882 comparison with remote sensing data. *Journal of Geophysical Research: Atmospheres*,
883 *119*(10), 6259–6277. https://doi.org/10.1002/2013JD021099
884 Klingmüller, K., Pozzer, A., Metzger, S., Stenchikov, G. L., & Lelieveld, J. (2016). Aerosol optical
885 depth trend over the Middle East. *Atmospheric Chemistry and Physics*, *16*(8), 5063–
886 5073. https://doi.org/10.5194/acp-16-5063-2016
887 Kokkalis, P., K. Al Jassar, H., Solomos, S., Raptis, P.-I., Al Hendi, H., Amiridis, V., et al. (2018).
888 Long-Term Ground-Based Measurements of Aerosol Optical Depth over Kuwait City.
889 *Remote Sensing*, *10*(11), 1807. https://doi.org/10.3390/rs10111807
890 Kuciauskas, A. P., Xian, P., Hyer, E. J., Oyola, M. I., & Campbell, J. R. (2018). Supporting Weather
891 Forecasters in Predicting and Monitoring Saharan Air Layer Dust Events as They Impact
892 the Greater Caribbean. *Bulletin of the American Meteorological Society*, *99*(2), 259–268.
893 https://doi.org/10.1175/BAMS-D-16-0212.1
894 Kumar, K. R., Attada, R., Dasari, H. P., Vellore, R. K., Langodan, S., Abualnaja, Y. O., & Hoteit, I.
895 (2018). Aerosol Optical Depth variability over the Arabian Peninsula as inferred from
896 satellite measurements. *Atmospheric Environment*, *187*, 346–357.
897 https://doi.org/10.1016/j.atmosenv.2018.06.011
898 Kumar, R., Barth, M. C., Pfister, G. G., Naja, M., & Brasseur, G. P. (2014). WRF-Chem simulations
899 of a typical pre-monsoon dust storm in northern India: influences on aerosol optical
900 properties and radiation budget. *Atmospheric Chemistry and Physics*, *14*(5), 2431–2446.
901 https://doi.org/10.5194/acp-14-2431-2014

902 Lee, J. A., Jiménez, P. A., Gueymard, C. A., & Nguyen, N. (2021). Dataset: Middle East AOD550
903 Forecasts & Observations, 2018–2019. Retrieved March 9, 2021, from
904 https://dashrepo.ucar.edu/dataset/187_jaredlee.html
905 Levin, Z., Teller, A., Ganor, E., & Yin, Y. (2005). On the interactions of mineral dust, sea-salt
906 particles, and clouds: A measurement and modeling study from the Mediterranean
907 Israeli Dust Experiment campaign. *Journal of Geophysical Research: Atmospheres*,
908 *110*(D20). https://doi.org/10.1029/2005JD005810
909 Li, C., Hsu, N. C., & Tsay, S.-C. (2011). A study on the potential applications of satellite data in air
910 quality monitoring and forecasting. *Atmospheric Environment*, *45*(22), 3663–3675.
911 https://doi.org/10.1016/j.atmosenv.2011.04.032
912 Liu, M., Westphal, D. L., Wang, S., Shimizu, A., Sugimoto, N., Zhou, J., & Chen, Y. (2003). A high-
913 resolution numerical study of the Asian dust storms of April 2001. *Journal of Geophysical*
914 *Research: Atmospheres*, *108*(D23). https://doi.org/10.1029/2002JD003178
915 Lu, C.-H., Silva, A. da, Wang, J., Moorthi, S., Chin, M., Colarco, P., et al. (2016). The
916 implementation of NEMS GFS Aerosol Component (NGAC) Version 1.0 for global dust
917 forecasting at NOAA/NCEP. *Geoscientific Model Development*, *9*(5), 1905–1919.
918 https://doi.org/10.5194/gmd-9-1905-2016
919 Lude, S., Fluri, T. P., Alhajraf, S., Jülch, V., Kühn, P., Marful, A., & Contreras, J. R. S. (2015).
920 Optimization of the Technology Mix for the Shagaya 2 GW Renewable Energy Park in
921 Kuwait. *Energy Procedia*, *69*, 1633–1642. https://doi.org/10.1016/j.egypro.2015.03.120
922 Mangold, A., Backer, H. D., Paepe, B. D., Dewitte, S., Chiapello, I., Derimian, Y., et al. (2011).
923 Aerosol analysis and forecast in the European Centre for Medium-Range Weather

924 Forecasts Integrated Forecast System: 3. Evaluation by means of case studies. *Journal of*
925 *Geophysical Research: Atmospheres*, *116*(D3). https://doi.org/10.1029/2010JD014864
926 Mas'ud, A. A., Wirba, A. V., Alshammari, S. J., Muhammad-Sukki, F., Abdullahi, M. M.,
927 Albarracín, R., & Hoq, M. Z. (2018). Solar Energy Potentials and Benefits in the Gulf
928 Cooperation Council Countries: A Review of Substantial Issues. *Energies*, *11*(2), 372.
929 https://doi.org/10.3390/en11020372
930 de Meij, A., Pozzer, A., & Lelieveld, J. (2012). Trend analysis in aerosol optical depths and
931 pollutant emission estimates between 2000 and 2009. *Atmospheric Environment*, *51*,
932 75–85. https://doi.org/10.1016/j.atmosenv.2012.01.059
933 Menut, L., Rea, G., Mailler, S., Khvorostyanov, D., & Turquety, S. (2015). Aerosol forecast over
934 the Mediterranean area during July 2013 (ADRIMED/CHARMEX). *Atmospheric Chemistry*
935 *and Physics*, *15*(14), 7897–7911. https://doi.org/10.5194/acp-15-7897-2015
936 Middleton, N. J. (2017). Desert dust hazards: A global review. *Aeolian Research*, *24*, 53–63.
937 https://doi.org/10.1016/j.aeolia.2016.12.001
938 Modarres, R., & Sadeghi, S. (2018). Spatial and temporal trends of dust storms across desert
939 regions of Iran. *Natural Hazards*, *90*(1), 101–114. https://doi.org/10.1007/s11069-017-
940 3035-8
941 Molod, A., Takacs, L., Suarez, M., & Bacmeister, J. (2015). Development of the GEOS-5
942 atmospheric general circulation model: evolution from MERRA to MERRA2. *Geoscientific*
943 *Model Development*, *8*(5), 1339–1356. https://doi.org/10.5194/gmd-8-1339-2015
944 Morcrette, J.-J., Boucher, O., Jones, L., Salmond, D., Bechtold, P., Beljaars, A., et al. (2009).
945 Aerosol analysis and forecast in the European Centre for Medium-Range Weather

946 Forecasts Integrated Forecast System: Forward modeling. *Journal of Geophysical*
947 *Research: Atmospheres*, *114*(D6). https://doi.org/10.1029/2008JD011235
948 Munawwar, S., & Ghedira, H. (2014). A review of Renewable Energy and Solar Industry Growth
949 in the GCC Region. *Energy Procedia*, *57*, 3191–3202.
950 https://doi.org/10.1016/j.egypro.2015.06.069
951 Nabat, P., Solmon, F., Mallet, M., Kok, J. F., & Somot, S. (2012). Dust emission size distribution
952 impact on aerosol budget and radiative forcing over the Mediterranean region: a
953 regional climate model approach. *Atmospheric Chemistry and Physics*, *12*(21), 10545–
954 10567. https://doi.org/10.5194/acp-12-10545-2012
955 Najafpour, N., Afshin, H., & Firoozabadi, B. (2018). The 20–22 February 2016 Mineral Dust Event
956 in Tehran, Iran: Numerical Modeling, Remote Sensing, and In Situ Measurements.
957 *Journal of Geophysical Research: Atmospheres*, *123*(10), 5038–5058.
958 https://doi.org/10.1029/2017JD027593
959 Osipov, S., & Stenchikov, G. (2018). Simulating the Regional Impact of Dust on the Middle East
960 Climate and the Red Sea. *Journal of Geophysical Research: Oceans*, *123*(2), 1032–1047.
961 https://doi.org/10.1002/2017JC013335
962 Ou, S. S.-C., Liou, K.-N., Wang, X., Hansell, R., Lefevre, R., & Cocks, S. (2009). Satellite remote
963 sensing of dust aerosol indirect effects on ice cloud formation. *Applied Optics*, *48*(3),
964 633–642. https://doi.org/10.1364/AO.48.000633
965 Pérez, C., Nickovic, S., Pejanovic, G., Baldasano, J. M., & Özsoy, E. (2006). Interactive dust-
966 radiation modeling: A step to improve weather forecasts. *Journal of Geophysical*
967 *Research: Atmospheres*, *111*(D16). https://doi.org/10.1029/2005JD006717

968 Pérez, C., Haustein, K., Janjic, Z., Jorba, O., Huneeus, N., Baldasano, J. M., et al. (2011).
969 Atmospheric dust modeling from meso to global scales with the online NMMB/BSC-Dust
970 model – Part 1: Model description, annual simulations and evaluation.
971 *Atmospheric Chemistry and Physics*, *11*(24), 13001–13027. https://doi.org/10.5194/acp-
972 11-13001-2011
973 Poudineh, R., Sen, A., & Fattouh, B. (2018). Advancing renewable energy in resource-rich
974 economies of the MENA. *Renewable Energy*, *123*, 135–149.
975 https://doi.org/10.1016/j.renene.2018.02.015
976 Powers, J. G., Klemp, J. B., Skamarock, W. C., Davis, C. A., Dudhia, J., Gill, D. O., et al. (2017). The
977 Weather Research and Forecasting Model: Overview, System Efforts, and Future
978 Directions. *Bulletin of the American Meteorological Society*, *98*(8), 1717–1737.
979 https://doi.org/10.1175/BAMS-D-15-00308.1
980 Prospero, J. M., Landing, W. M., & Schulz, M. (2010). African dust deposition to Florida:
981 Temporal and spatial variability and comparisons to models. *Journal of Geophysical*
982 *Research: Atmospheres*, *115*(D13). https://doi.org/10.1029/2009JD012773
983 Querol, X., Tobías, A., Pérez, N., Karanasiou, A., Amato, F., Stafoggia, M., et al. (2019).
984 Monitoring the impact of desert dust outbreaks for air quality for health studies.
985 *Environment International*, *130*, 104867. https://doi.org/10.1016/j.envint.2019.05.061
986 Rémy, S., Benedetti, A., Bozzo, A., Haiden, T., Jones, L., Razinger, M., et al. (2015). Feedbacks of
987 dust and boundary layer meteorology during a dust storm in the eastern
988 Mediterranean. *Atmospheric Chemistry and Physics*, *15*(22), 12909–12933.
989 https://doi.org/10.5194/acp-15-12909-2015

990 Rémy, S., Kipling, Z., Flemming, J., Boucher, O., Nabat, P., Michou, M., et al. (2019). Description
991 and evaluation of the tropospheric aerosol scheme in the European Centre for Medium-
992 Range Weather Forecasts (ECMWF) Integrated Forecasting System (IFS-AER, cycle 45R1).
993 *Geoscientific Model Development*, *12*(11), 4627–4659. https://doi.org/10.5194/gmd-12-
994 4627-2019
995 Rienecker, M. M., Suarez, M. J., Todling, R., Bacmeister, J., Takacs, L., Liu, H.-C., et al. (2008).
996 *The GEOS-5 Data Assimilation System-Documentation of Versions 5.0.1, 5.1.0, and 5.2.0*
997 (Technical Report Series on Global Modeling and Data Assimilation, Volume 27 No.
998 NASA/TM-2008-104606-VOL-27). NASA. Retrieved from
999 https://ntrs.nasa.gov/search.jsp?R=20120011955
1000 Rubin, J. I., Reid, J. S., Hansen, J. A., Anderson, J. L., Holben, B. N., Xian, P., et al. (2017).
1001 Assimilation of AERONET and MODIS AOT observations using variational and ensemble
1002 data assimilation methods and its impact on aerosol forecasting skill. *Journal of*
1003 *Geophysical Research: Atmospheres*, *122*(9), 4967–4992.
1004 https://doi.org/10.1002/2016JD026067
1005 Saeed, T. M., Al-Dashti, H., & Spyrou, C. (2014). Aerosol's optical and physical characteristics
1006 and direct radiative forcing during a shamal dust storm, a case study. *Atmospheric*
1007 *Chemistry and Physics*, *14*(7), 3751–3769. https://doi.org/10.5194/acp-14-3751-2014
1008 Salam, M. A., & Khan, S. A. (2017). Transition towards sustainable energy production – A review
1009 of the progress for solar energy in Saudi Arabia: *Energy Exploration & Exploitation*.
1010 https://doi.org/10.1177/0144598717737442

1011 Seznec, J.-F. (2018). *Renewable energy in the Middle East*. Washington, DC: Atlantic Council.
1012 Retrieved from https://www.atlanticcouncil.org/in-depth-research-
1013 reports/report/renewable-energy-in-the-middle-east/
1014 Shao, Y., Wyrwoll, K.-H., Chappell, A., Huang, J., Lin, Z., McTainsh, G. H., et al. (2011). Dust cycle:
1015 An emerging core theme in Earth system science. *Aeolian Research*, *2*(4), 181–204.
1016 https://doi.org/10.1016/j.aeolia.2011.02.001
1017 Sharma, D., Singh, D., & Kaskaoutis, D. G. (2012). Impact of Two Intense Dust Storms on Aerosol
1018 Characteristics and Radiative Forcing over Patiala, Northwestern India. *Advances in*
1019 *Meteorology*, *2012*, 956814. https://doi.org/10.1155/2012/956814
1020 Smirnov, A., Holben, B. N., Eck, T. F., Dubovik, O., & Slutsker, I. (2000). Cloud-Screening and
1021 Quality Control Algorithms for the AERONET Database. *Remote Sensing of Environment*,
1022 *73*(3), 337–349. https://doi.org/10.1016/S0034-4257(00)00109-7
1023 Thompson, G., & Eidhammer, T. (2014). A Study of Aerosol Impacts on Clouds and Precipitation
1024 Development in a Large Winter Cyclone. *Journal of the Atmospheric Sciences*, *71*(10),
1025 3636–3658. https://doi.org/10.1175/JAS-D-13-0305.1
1026 Uno, I., Eguchi, K., Yumimoto, K., Takemura, T., Shimizu, A., Uematsu, M., et al. (2009). Asian
1027 dust transported one full circuit around the globe. *Nature Geoscience*, *2*(8), 557–560.
1028 https://doi.org/10.1038/ngeo583
1029 Wagner, A., Blechschmidt, A.-M., Bouarar, I., Brunke, E.-G., Clerbaux, C., Cupeiro, M., et al.
1030 (2015). Evaluation of the MACC operational forecast system – potential and challenges
1031 of global near-real-time modelling with respect to reactive gases in the troposphere.

Atmospheric Chemistry and Physics, *15*(24), 14005–14030. https://doi.org/10.5194/acp-15-14005-2015

Wang, J., Bhattacharjee, P. S., Tallapragada, V., Lu, C.-H., Kondragunta, S., Silva, A. da, et al. (2018). The implementation of NEMS GFS Aerosol Component (NGAC) Version 2.0 for global multispecies forecasting at NOAA/NCEP – Part 1: Model descriptions. *Geoscientific Model Development*, *11*(6), 2315–2332. https://doi.org/10.5194/gmd-11-2315-2018

Xu, Y. (2018). Evaluation of mineral dust aerosol optical depth and related components from the CHIMERE-DUST model using satellite remote sensing and ground-based observations. *Atmospheric Environment*, *191*, 395–413. https://doi.org/10.1016/j.atmosenv.2018.03.061

Yoon, J., Hoyningen-Huene, W. von, Kokhanovsky, A. A., Vountas, M., & Burrows, J. P. (2012a). Corrigendum to "Trend analysis of aerosol optical thickness and Ångström exponent derived from the global AERONET spectral observations" published in Atmos. Meas. Tech., 5, 1271–1299, 2012. *Atmospheric Measurement Techniques*, *5*(9), 2113–2113. https://doi.org/10.5194/amt-5-2113-2012

Yoon, J., Hoyningen-Huene, W. von, Kokhanovsky, A. A., Vountas, M., & Burrows, J. P. (2012b). Trend analysis of aerosol optical thickness and Ångström exponent derived from the global AERONET spectral observations. *Atmospheric Measurement Techniques*, *5*(6), 1271–1299. https://doi.org/10.5194/amt-5-1271-2012

Yu, H., Remer, L. A., Chin, M., Bian, H., Tan, Q., Yuan, T., & Zhang, Y. (2012). Aerosols from Overseas Rival Domestic Emissions over North America. *Science*, *337*(6094), 566–569. https://doi.org/10.1126/science.1217576

Yu, S., Eder, B., Dennis, R., Chu, S.-H., & Schwartz, S. E. (2006). New unbiased symmetric metrics for evaluation of air quality models. *Atmospheric Science Letters*, *7*(1), 26–34. https://doi.org/10.1002/asl.125

Yu, Y., Notaro, M., Kalashnikova, O. V., & Garay, M. J. (2016). Climatology of summer Shamal wind in the Middle East. *Journal of Geophysical Research: Atmospheres*, *121*(1), 289–305. https://doi.org/10.1002/2015JD024063

Zhang, Y., Liu, Y., Kucera, P. A., Alharbi, B. H., Pan, L., & Ghulam, A. (2015). Dust modeling over Saudi Arabia using WRF-Chem: March 2009 severe dust case. *Atmospheric Environment*, *119*, 118–130. https://doi.org/10.1016/j.atmosenv.2015.08.032

Zhao, C., Liu, X., Ruby Leung, L., & Hagos, S. (2011). Radiative impact of mineral dust on monsoon precipitation variability over West Africa. *Atmospheric Chemistry and Physics*, *11*(5), 1879–1893. https://doi.org/10.5194/acp-11-1879-2011